THE ASTROPHYSICAL JOURNAL, 456:811–832, 1996 January 10

ANALYSIS OF THE LATE OPTICAL SPECTRA OF SN 1993J

JOHN C. HOUCK[1] AND CLAES FRANSSON
Stockholm Observatory, S-133 36 Saltsjöbaden, Sweden
Received 1995 January 16; accepted 1995 July 20

ABSTRACT

We have used a detailed non-LTE synthetic spectrum code to interpret Royal Greenwich Observatory archive spectra from the nebular phase of SN 1993J. In general, we obtain good agreement between the observed optical spectra and synthetic spectra based on the helium star explosion model 4H 47 of Nomoto et al., corresponding to a 3.2 $M_\odot$ helium core with 0.08 $M_\odot$ of ^{56}Ni. The fit to the observed spectrum is improved when some of the iron-rich material is macroscopically mixed outward to a velocity of at least 3000 km s^{-1}, and when some of the oxygen-rich material is mixed inward to $\sim$1000 km s^{-1}. We find that the observed spectra are consistent with a symmetric explosion in which $\sim$0.5 $M_\odot$ of oxygen occupies a spherical shell between 1000–4000 km s^{-1}. Observations interpreted earlier as evidence for large asymmetries are better explained by line blending effects. In particular, scattering of [O I] $\lambda\lambda$6300, 6364 by Hα in the hydrogen envelope strongly affects the [O I] profile. The width of the Hα absorption feature constrains the velocity thickness of the hydrogen envelope, while the observed time evolution of this feature indicates that Hα became optically thin in 1993 October, constraining the hydrogen density. From these constraints and the observed Hα luminosity and line width, we conclude that the H/He envelope mass is 0.2–0.4 $M_\odot$ and that the bulk of this mass lies between 8500–10,000 km s^{-1}. The envelope is significantly helium enriched. After $\sim$350 days, an additional power source is necessary to reproduce the observed Hα luminosity. It is likely that X-rays from the circumstellar interaction provide the necessary energy input.

Subject headings: stars: interiors — supernovae: individual (SN 1993J)

1. INTRODUCTION

SN 1993J was discovered on 1993 March 28 (Garcia 1993), probably within a day after the explosion, with the epoch of core collapse close to March 27.8 (Wheeler et al. 1993; Woosley et al. 1994; Shigeyama et al. 1994). Much of the early observational and theoretical work on SN 1993J was summarized by Wheeler & Filippenko (1993). Lewis et al. (1994) discuss the photometric and spectroscopic evolution of the supernova using observations obtained from La Palma over the first 125 days. Because the distance to the parent galaxy (M81) is accurately known from Cepheid variable measurements, absolute measurements of the energetics of this supernova can be much more precise than is usually possible. Throughout this paper, we adopt 3.5 Mpc as the distance to the supernova (Freedman et al. 1993). We correct for reddening using the extinction curve of Cardelli, Clayton, & Mathis (1989) with $E(B-V) = 0.18$ (Fransson & Sonneborn 1994) and $R_V = 3.1$.

The early rise and rapid decline in bolometric luminosity have been interpreted by several authors as the release of shock-deposited energy from the supernova, leading to the conclusion that the H/He envelope mass was smaller than 0.5 $M_\odot$ (Podsiadlowski et al. 1993; Shigeyama et al. 1994; Wheeler et al. 1993; Woosley et al. 1994). Because of the relatively small envelope mass, the expansion velocity was larger than usual for a Type II supernova. During the first 5 days, the photosphere expanded at 13,000 km s^{-1}, while in early April, the blueward edge of the absorption component of the Hα profile indicated an expansion velocity of $\sim$19,000 km s^{-1} (Lewis et al. 1994). Between an age of 9 days and 21 days, the bolometric luminosity rose to a second peak, associated with the escape of thermal energy from the decay of ^{56}Ni and ^{56}Co. The luminosity at this second peak was well reproduced in models with $\sim$0.1 $M_\odot$ of ^{56}Ni (Podsiadlowski et al. 1993; Shigeyama et al. 1994; Wheeler et al. 1993; Woosley et al. 1994).

From day 21 to day 50, the luminosity declined again. This second decline has been attributed to the recombination front reaching the boundary between the H/He envelope and the He mantle. Because the material in the He mantle had recombined by the time the recombination front arrived, the photosphere moved rapidly inward through the mantle, and the observed spectrum became increasingly nebular. During this phase, the character of the optical spectrum changed dramatically, from that of a Type II supernova with strong Hα emission to that of a Type "IIb" supernova with strong He lines, but with no obvious hydrogen emission (Filippenko, Matheson, & Ho 1993; Lewis et al. 1994). After day 50, the bolometric luminosity declined exponentially with an e-folding time of 54 days. This decay timescale is significantly shorter than the ^{56}Co decay time, probably because of the rapid escape of gamma rays from radioactive decay; detailed light-curve models fit this behavior with a ^{56}Ni mass of 0.075 M (Podsiadlowski et al. 1993; Shigeyama et al. 1994; Wheeler et al. 1993; Woosley et al. 1994). Shigeyama et al. (1994) also find that the double-peaked light curve is best fit by models with some mixing of ^{56}Ni into the He mantle.

While the early behavior of the SN 1993J light curve and spectra has been reasonably well fit by spherically symmetric helium star explosion models, many uncertainties remain. A better determination of the hydrogen envelope mass would help to understand the evolutionary history of the progenitor star and may indicate whether or not mass loss to a binary companion is necessary to explain the low envelope mass. An observational determination of the oxygen mass would be par-

[1] Present address: University of Michigan, Department of Astronomy, Dennison Building, Ann Arbor, MI 48109-1090.

ticularly useful, as this would provide a sensitive indicator of the core mass of the progenitor star (Nomoto et al. 1993). Observational evidence on the degree of mixing in the ejecta is of great interest because this evidence would place valuable constraints on the hydrodynamic interactions which occur in the explosion. The polarization of the emission from SN 1993J is not well understood, although spectropolarimetry indicates that the supernova is intrinsically asymmetric in some way (Smith 1993; Trammell, Hines, & Wheeler 1993).

Spyromilio (1994) identifies features of Mg I] λ4571, [O I] λ5577, and [O I] $\lambda\lambda$6300, 6364 and interprets their shapes as evidence for clumping and significant large-scale asymmetry in the ejecta. He concludes that the bulk of the oxygen emission comes from a region which is blueshifted by $\sim$2000 km s^{-1}. Instead, Filippenko, Matheson, & Barth (1994) suggested that the large blueshifts are a consequence of viewing primarily the near side of the optically thick ejecta. Similarly, Wang & Hu (1994) suggest that the apparent blueshifts of the oxygen lines at age $\sim$120 days arise because, in the clumpy ejecta, the receding clumps are hidden by the photosphere, while the approaching (blueshifted) clumps are visible either because hydrodynamic mixing has driven clumps above the photosphere or because their presence on the near side of the nebula places them at low optical depth. In keeping with this model, they predict that the oxygen lines should shift back toward line center as the supernova evolves and the optical depth decreases as a result of expansion.

While these apparently blueshifted oxygen lines have attracted great attention, we would like to point out several problems with this explanation. First, while concentrating on the apparently large blueshifts seen in Mg I] λ4571, [O I] λ5577, and [O I] $\lambda\lambda$6300, 6364, none of these groups explain the absence of a large blueshifts in the O I λ7771 and O I λ9264 lines. In explaining the blueshifts as a consequence of viewing primarily the near side of the optically thick ejecta, it is difficult to see why this absorption, presumably caused by electron scattering, should so strongly affect four widely separated lines (4571, 5577, 6300, and 6364) but have a much weaker effect at 7771 Å and 9264 Å and no apparent affect on [Ca II] λ7307 or the Ca II IR triplet. The explanation forwarded by Spyromilio (1994) has a similar flaw; if the oxygen-emitting material is strongly asymmetric on large scales, this should be apparent in the lines at 7771 Å and 9264 Å. Second, despite the factor of $>$60 decrease in mean density between age 100 days and age 400 days, no redward shift of the oxygen lines (as predicted by Wang & Hu 1994) has been seen. Since the photosphere had already begun to recede at age 100 days, this absence of a redward shift (toward line center) effectively rules out this model. Furthermore, detailed models (Baron et al. 1995; Woosley et al. 1994), including our own, indicate that the photosphere had probably receded to the deep interior of the ejecta by 1993 July ($\sim$100 days) so that broadband absorption of the red wing of the oxygen emission lines (see also Filippenko et al. 1994) is not a viable explanation for the observed lines. While the ejecta are probably quite clumpy, as mentioned by Wang & Hu (1994) and Filippenko et al. (1994), the apparent blueshifts are probably a result of line blending rather than broadband absorption, as we discuss in detail.

Patat, Chugai, & Mazzali (1995) discuss the late-time Hα emission from SN 1993J. In particular, they find that the observed emission can be described by a shell of hydrogen emitting material between 7500–11,400 km s^{-1}, and that energy deposition by gamma rays from radioactive decay of 0.075 $M_\odot$ of ^{56}Ni is insufficient to explain the observed Hα flux after age 150 days. Instead, they suggest that the Hα emission is powered by X-rays from the circumstellar interaction. Their computation of the Hα flux up to age 150 days does not include Balmer continuum photoionization caused by UV photons from the interior of the nebula, nor does it include the scattering of [O I] $\lambda\lambda$6300, 6364 photons by Hα in the H/He envelope. We show that these two effects play an dominant role in producing the observed Hα emission. As a result, the decay of ^{56}Ni in the interior of the nebula indeed provides the ultimate power source for Hα emission up to about age 250 days, as is consistent with the observed agreement between the slope of the Hα light curve and the expected ^{56}Co decay curve up to this epoch (Fig. 3). In contrast, it is difficult to see why a circumstellar power source should so closely mimic the ^{56}Co decay curve between 150–250 days. Nevertheless, the emergence of strong Hα emission after age 250 days provides clear evidence for circumstellar interaction at late times.

As the spectrum evolves further into its nebular phase, optical depth effects become less severe, and the problem of extracting information from the observed spectrum is greatly simplified. Because the ejecta are more transparent, it becomes possible to extract information on the whole interior structure of the nebula (Fransson & Chevalier 1989). Using a non-LTE synthetic spectrum code, we have investigated in detail the formation of the nebular phase spectrum. We find that the observed spectra are consistent with a spherically symmetric distribution of material, and we are able to place limits on the masses of oxygen and hydrogen which are likely to be present. The explosion models used in our calculations are described in § 2. We describe our synthetic spectrum code in § 3 and discuss the observed spectra in § 4. Our synthetic spectrum calculations are discussed in §§ 5–7, and our conclusions are presented in § 8.

2. EXPLOSION MODELS

The helium star explosion model 4H 47 of Nomoto et al. (1993) formed the basis for most of our work on the spectrum of SN 1993J (Fig. 1). This model corresponds to a helium core of 4.0 $M_\odot$, including the neutron star mass of 1.35 $M_\odot$, and it produces $\sim$0.5 $M_\odot$ of oxygen. Outside the helium core, the hydrogen envelope contains 0.5 $M_\odot$, resulting in a total ejecta mass of 3.2 $M_\odot$. Because the ^{56}Ni mass produced in this explosion model was too large to be consistent with the light curve models of Shigeyama et al. (1994), we shifted the mass cut associated with neutron star formation to reduce the ejected ^{56}Ni mass to 0.08 $M_\odot$. A similar procedure was used by Shigeyama et al. (1994). This ^{56}Ni mass was sufficient to reproduce the overall flux level in the optical spectrum. To agree better with the narrower line peaks in the observed spectrum, the velocity at the mass cut was shifted to 1000 km s^{-1}, slightly lowering the mean density in the model. With this mass cut, the region inside 1000 km s^{-1} is empty, and most of the ejecta lie in a shell between 1000 km s^{-1} and 10,000 km s^{-1}, with a velocity field $V \propto R$. A high-velocity tail of low-density material extends out to $\sim$40,000 km s^{-1} but contains less than $\sim$0.06 $M_\odot$, half of which is below 15,000 km s^{-1}. Most of the mass above $\sim$15,000 km s^{-1} is probably shocked to a high temperature, $\gtrsim 10^7$ K, by the interaction with the circumstellar medium (Fransson, Lundqvist, & Chevalier 1995) and is unlikely to contribute directly to the optical spectrum. However, X-ray emission from the circumstellar interaction

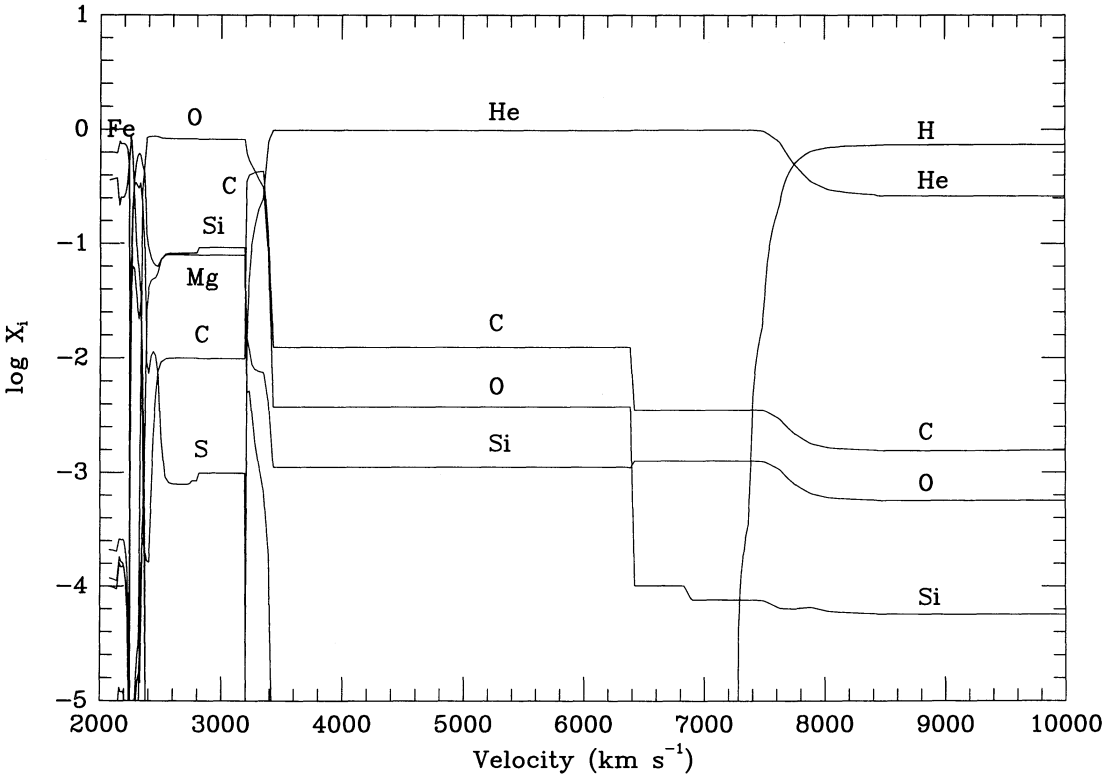

FIG. 1.—Composition of 4H 47 by number as a function of expansion velocity as computed by Nomoto et al. (1993).

does seem to provide the main power source for the observed Hα emission after ~350 days (Fransson & Houck 1995).

Model 3H 30 of Nomoto et al. (1993) was also considered. This model, which corresponds to a smaller helium core of 2.4 $M_\odot$, expands ~50% faster than 4H 47 and produces only 0.24 $M_\odot$ of oxygen. As in model 4H 47, the mass cut associated with neutron star formation was adjusted to make the ^{56}Ni mass agree with the light-curve models of Shigeyama et al. (1994). With this mass cut, the bulk of the ejecta occupied a shell between ~1000–15,000 km s^{-1}. All models assume a velocity field $V \propto R$, in excellent agreement with the hydrodynamic models of Shigeyama et al. (1994).

Because the explosion models of Nomoto et al. (1993) were constructed with much finer spatial resolution than our spectrum calculations can attain, we binned the models into ~25 constant density shells. The shell masses were selected so that the composition structure of the explosion model was well represented; composition mixing resulting from the binning procedure was avoided. To investigate the effect of macroscopic mixing on the observed spectrum, we altered the basic models in various ways. Macroscopic mixing was modeled by rearranging the radial shells, changing the shell volumes as necessary to produce a uniform mass density inside the mixed region. Clumping was modeled by moving shell boundaries to compress selected mass shells, producing a corresponding expansion in neighboring shells.

3. SPECTRUM MODEL

After the first few weeks, radioactive decay of ^{56}Co provides the main power source for the supernova. Roughly 96% of decays result in emission of gamma rays, with ~4% producing positrons. The gamma rays and positrons deposit their energy in the ejecta by ionizing and exciting atoms and ions and by heating the free electron gas. In our spectrum models, we used the spatial distribution of ^{56}Co to compute the gamma-ray flux incident on a given mass element by solving the transfer equation in a manner similar to that described by Swartz, Sutherland, & Harkness (1995), where the gamma-ray source function is determined by the concentration of ^{56}Co, and the opacity is determined by the gamma-ray absorption cross section, $\sigma_\gamma \approx 0.06 Z m_p$ cm^2, where Z is the nuclear charge and m_p is the proton mass. We assumed that the positron energy is deposited locally, according to the local concentration of ^{56}Co. Given the nonthermal energy input, we solved the Spencer-Fano equation (Kozma & Fransson 1991) self-consistently with the ionization equilibrium to determine the rates of nonthermal heating, ionization, and excitation. In computing the ionization balance, we also included photoionization by line and continuum photons emitted both locally and nonlocally. Collisional ionization was included for completeness but was unimportant. Both radiative and dielectric recombination processes were included. Atomic data sources are listed in the Appendix.

Our statistical equilibrium calculations treated H I, He I, C I–III, O I–III, Na I, Mg I–II, Si I–III, S I–III, Ca II, Fe I–V, and Co I–V as multilevel atoms. The three lowest ionization states of iron and cobalt were modeled with 100–120 energy levels each, although some calculations used an Fe II atom with 191 levels. The other atoms and ions were treated with two to 20 energy levels. In solving the rate equations, we include 992 transitions for Fe III, 1403 transitions for the smaller 121 level Fe II atom, and 1969 transitions for the larger 191 level Fe II atom. The spectra shown in the figures were computed using the larger Fe II model atom. Significantly fewer transitions are

used for the cobalt ions. Furthermore, we neglect the contribution from the many weak lines of iron peak ions which are important in the earlier photospheric phase; for further discussion of this point, see Baron & Hauschildt (1995). While this neglect may cause some of the smaller discrepancies between the observed and modeled spectra, it should not affect the stronger spectral features on which we base most of our conclusions. We feel this simplification is justified because these many weak lines probably do not dominate the formation of the optical spectrum in the nebular phase.

For each multilevel atom, we solved the non-LTE statistical equilibrium equations by multidimensional Newton-Raphson iteration. Excited states were populated by direct nonthermal excitation, thermal electron collisions, absorption of line photons, and recombination and depopulated by thermal electron collisions, emission of line photons, and photoionization. Two-photon continuum emission from the $2s\,^1S$ states of hydrogen and helium was included as well. Where excited state recombination coefficients were unavailable, we divided the total recombination rate between excited terms with most recombinations occurring via the higher excited states. For iron and cobalt ions, excited state recombination was restricted to the highest terms. Excited state photoionization was included for H II, He I, Mg I, O I, and Ca II. To speed the calculations, direct nonthermal excitation of excited states was included only in the hydrogen envelope and the helium mantle. In the other composition zones, $\lesssim 5\%$ of the nonthermal energy was absorbed in direct excitations. The radiation field in each line transition was evaluated using the Sobolev approximation, accounting for continuum absorption where necessary, using the prescription discussed by Hummer & Rybicki (1985). Iterative solution of the linearized statistical equilibrium equations for all multilevel atoms provided the collisional cooling rates which dominate the cooling.

The balance between nonthermal heating and collisional cooling determined the electron temperature. Unless otherwise stated, we will henceforth refer to the electron temperature as the temperature. Contributions from photoionization heating and recombination cooling were included for completeness but were generally small. We solved the ionization, excitation and thermal equilibrium equations iteratively to determine the steady state temperature in each mass shell self-consistently.

In each mass shell, the calculation was initialized by establishing ionization equilibrium at an assumed temperature, neglecting ionization by line photons. Having established the electron density, we solved the statistical equilibrium equations to obtain a first approximation to the excited state populations, assuming that allowed transitions were optically thick while all other transitions were optically thin. This provided an estimate of the rate of photoionization by line photons. With this photoionization rate, we reevaluated the ionization and statistical equilibrium.

With these initial values for the ion fractions and excited state populations, the statistical equilibrium equations were solved using a multidimensional Newton-Raphson iteration, computing the line optical depths self-consistently. After computing the total cooling rate, the temperature was corrected to improve the thermal equilibrium. Ionization equilibrium was then recomputed at the new temperature. Iteration continued until the thermal, statistical, and ionization equilibria converged, determining the temperature self-consistently. As long as the ionization equilibrium was not strongly coupled to the excitation equilibrium, this procedure converged quickly and accurately. The solution was considered to have achieved convergence when the fractional change in all variables was smaller than 10^{-3}. In some cases, usually for a few of the excited state level populations, this level of convergence could not be achieved, but in these isolated cases, the fractional change between iterations was generally smaller than 5%.

Having obtained the local solution for all mass shells, the nonlocal radiation field incident on each shell was computed from a formal solution of the transfer equation, using the Sobolev approximation to determine the mean intensity in each line transition (Swartz 1990). Aberration and advection effects are not included in this solution. In keeping with the Sobolev approximation, we consider only the mean intensity in a given line and make no reference to the intrinsic line profile other than to assume that the intrinsic line width is small compared to the Doppler shift across the nebula and that the Sobolev length is small compared to the distance over which physical conditions change. Thermal and statistical equilibrium was then reestablished in each shell, including the effects of the nonlocal radiation field. This global iteration accounted for the nonlocal coupling through the radiation field. The convergence characteristics of the transfer solution are described by Swartz (1990); generally speaking, the global iteration converges within five to 10 iterations. For clarity, we point out that our spectrum solution has no free parameters in the sense that they are used in the spectrum models of Baron et al. (1995). As discussed above, we do alter the structure of the input explosion model to test the effects of macroscopic mixing and clumping of the ejecta, but we introduce no other adjustable parameters.

Once the physical conditions in the nebula were established, the spectrum was computed, explicitly including line blending effects in the integration over the nebular volume. The integration was simplified by the nonrelativistic Sobolev approximation, in which the contribution to the observed flux at a particular frequency arises from a finite number of planar slabs in the nebula (assuming $V \propto R$ and neglecting relativistic effects; see Mihalas 1978, p. 471). When continuum absorption is unimportant, the flux at a particular frequency is

$$F_\nu = 2\pi \int_0^R p\,dp \sum_{j=1}^{N_\nu(p)} [1 - e^{-\tau_j(z_j, p)}] S_j(z_j, p) \times \exp\left[-\sum_{k=1}^{j-1} \tau_k(z_k, p) \right], \quad (1)$$

where $N_\nu(p)$ line transitions contribute at the observed frequency ν along a line of sight with impact parameter p. S_j and τ_j are the source function and Sobolev optical depth for transition j. Line emission and absorption affecting the flux observed at frequency ν are confined to planes of thickness equal to the Sobolev length and located at positions z_k along the line of sight, where z_k is determined by the Doppler shift. Features in the computed spectrum can be "de-blended" by a similar computation in which emission from only a single species is allowed, but in which all absorption processes are included.

4. DISCUSSION OF THE OBSERVED SPECTRA

Before discussing our spectrum calculations, we use the observed spectra directly to constrain the structure and physical conditions in the supernova. While this approach has severe limitations, several valuable constraints do emerge. The confidence with which one can interpret spectral features

depends on the extent of line blending in the selected features. Our interpretation is based primarily on the data and does not reflect particular detailed calculations. However, we have tried to judge the degree of line blending present based on the experience we have gained from our synthetic spectrum calculations.

4.1. *140 Days*

In the optical spectrum at age 140 days (1993 August 15) (Fig. 2), the prominent features at 7771 Å and at 9264 Å are recombination lines of O I. Because these lines are relatively unblended, they provide information on the range of velocities occupied by O I. At 140 days, the centroid of the O I λ7771 line is blueshifted by $\sim$450 km s^{-1}, while its red edge is blended with Fe I emission. The flat-topped line profile is consistent with emission from a shell; the unblended blue edge indicates a maximum expansion velocity of $\sim$4000 km s^{-1}, while the half-width of the flat top indicates an expansion velocity of $\sim$1000 km s^{-1} at its inner edge. The O I λ9264 line also shows a slight blueshift of $\sim$360 km s^{-1}, while its red edge is blended with iron and cobalt emission. The blue edge seems unblended and is consistent with oxygen being confined to velocities below $\sim$4000 km s^{-1}, although the velocity deduced from the 9264 Å feature is somewhat lower.

The emission feature centered at 5546 Å has been attributed to [O I] λ5577 by Lewis et al. (1994), Spyromilio (1994), and others. Because the centroid of the feature is blueshifted by $\sim$1700 km s^{-1} relative to [O I] λ5577, Spyromilio interprets this as evidence for a large asymmetry in the nebula. However, because the O I recombination features do not show similar Doppler shifts, this explanation seems unlikely. Because [O I] λ5577 lies near the edge of the forest of Fe lines between 4000–5500 Å, blending with iron lines presents a more plausible explanation. Further evidence for line blending comes from comparison of the shapes of the [O I] $\lambda\lambda$6300, 6364, O I λ9264, and O I λ7771 profiles with the [O I] λ5577 profile. The latter has a very narrow, $\lesssim$150 km s^{-1} wide peak, while the others have much broader profiles $\sim$1000 km s^{-1} wide. At best, therefore, the 5546 Å feature provides only an upper limit to the brightness of O I λ5577, so that $I(6300)/I(5577) \gtrsim 3.1$ at 140 days.

Taking the brightness of the 5546 Å feature as an upper limit to the [O I] λ5577 flux, we can estimate the temperature in the oxygen-emitting material. If the O I lines at 6300 Å, 6364 Å, and 5577 Å are formed mainly by collisional excitation, the ratio $I(6300)/I(5577)$ is

$$\frac{\mathrm{I}(6300)}{\mathrm{I}(5577)} = 0.03\beta_{6300} \times \left[1 + 1.44T_3^{-0.034}\left(\frac{n_e}{10^8\ \mathrm{cm}^{-3}}\right)^{-1}\right] e^{25.83/T_3}, \quad (2)$$

where n_e is the electron density and T_3 is the temperature in units of 10^3 K. Here β_{6300} is the Sobolev escape probability of [O I] λ6300. An upper limit on the temperature follows from assuming $\tau_{6300} \ll 1$, so that $\beta_{6300} \approx 1$. If $n_e = 10^9$ cm^{-3}, we

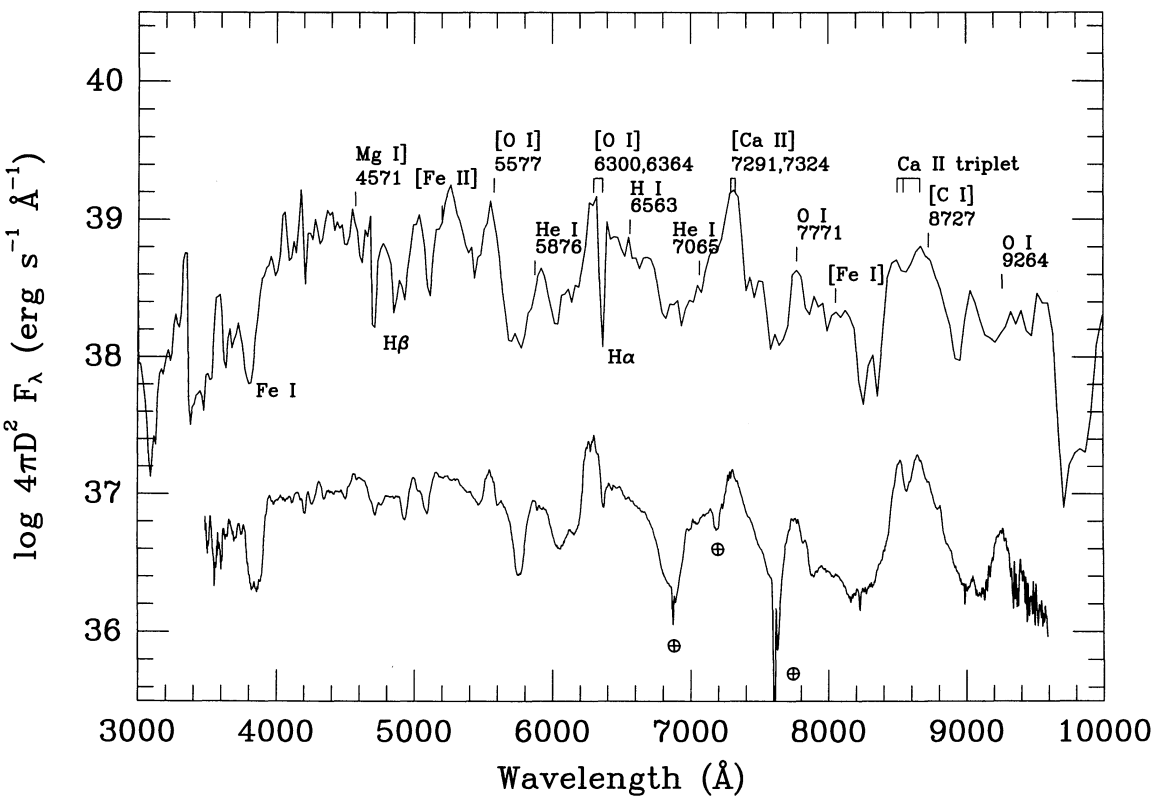

FIG. 2.—Line identifications marked on the computed spectrum at age 140 days (shifted upward by +1.5 dex for clarity) compared with the observed spectrum from 1993 August 15 (*lower curve*). In the computed spectrum, iron emission features are overproduced, contributing to the excessive emission at Hα . Also, the computed spectrum shows stronger Hα and Hβ absorption features than are present in the observed spectrum. The apparent blueshift of the [O I] λ5577 feature in the computed spectrum is the result of blending with iron and cobalt emission.

obtain $T \lesssim 5700$ K, whereas $n_e = 10^8$ cm^{-3} yields $T \lesssim 6700$ K. Therefore, the observed limit on the ratio $I(6300)/I(5577)$ indicates that the temperature of the O I–emitting region was $T \lesssim 6700$ K at 140 days, weakly dependent on the electron density.

While the ejecta likely contain a significant mass of helium, it contributes few strong spectral features. At 140 days, at least part of the feature at 5900 Å was attributable to He I λ5876, although the centroid of the feature was shifted ~ 1400 km s^{-1} redward. This shift was probably the result of a blend with Na I $\lambda\lambda$5890, 5896 and Fe I λ5958 emission rather than an intrinsic asymmetry in the nebula. Assuming the nebula was symmetric, the apparently unblended blue wing of this feature yields an expansion velocity of only 5000 km s^{-1}. In contrast, explosion models place much of the helium mass at significantly higher velocities. This indicates that gamma-ray deposition in the helium mantle above 5000 km s^{-1} was inefficient. In this case, the luminosity of the helium lines yields only a lower limit to the helium mass.

The broad feature at 8600 Å is a blend of [C I] λ8727 and Ca II triplet emission, while the feature at 7200 Å is a blend of [Ca II] λ7307 and He I λ7065. The relatively sharp profiles in the [Ca II] λ7307 and Ca II IR triplet features seen at 140 days indicate that calcium was present at very low velocities ($\ll 1000$ km s^{-1}). In spherically symmetric helium star explosion models, most of the calcium, a product of explosive nucleosynthesis, lies in a thin shell just outside the iron core with velocity $\gtrsim 1000$ km s^{-1}. Therefore, the sharp profiles of the observed Ca lines are an indication that mixing has occurred since core collapse. The interpretation of the remaining spectral features between 4000–5000 Å is much more uncertain because of the extensive blending of many absorption and emission features of Fe, Co, Mg I, and He I.

4.2. *284 Days*

By age 284 days (1994 January 5), the optical emission was dominated by [O I] $\lambda\lambda$6300, 6364, [Ca II] λ7307, and Mg I] λ4571. The feature near [O I] λ5577 weakened so that the ratio $I(6300)/I(5577) \lesssim 16$, indicating that the temperature in the oxygen-emitting material had decreased to $T \lesssim 4200$–4800 K depending on the electron density. The O I recombination lines at 9264 Å and 7771 Å also weakened significantly relative to [O I] $\lambda\lambda$6300, 6364, although the ratio $I(9264)/I(7771)$ remained constant. This ratio is expected to remain constant because it is determined mainly by the ratio of the effective rates of recombination to the $3d\,^5D$ and $3p\,^5P$ excited states of O I (§ 6.3). The Ca II line ratio $I(7307)/I(8582)$ increased from ~ 1 to $I(7307)/I(8582) \gtrsim 3$, indicating that the calcium emitting region was also much cooler at this epoch than at 140 days.

4.3. *416 Days*

The presence of strong Hα emission is the most obvious change in the spectrum at 416 days (1994 May 17). Figure 3 shows that the Hα luminosity declines roughly $\propto t^{-2}e^{-t/111\ \mathrm{days}}$, consistent with radioactive decay as the primary power source (although see § 6.1.2), but that $L_{\mathrm{H}\alpha}$ is roughly constant after age 300 days, indicating that energy input from the circumstellar interaction has become important in the H/He envelope (Chevalier & Fransson 1994; Fransson & Houck 1995; Patat et al. 1995; Filippenko et al. 1994). At this epoch, the optical spectrum is still dominated by [O I] $\lambda\lambda$6300, 6364, [Ca II] λ7307, and Mg I] λ4571, although broader features between 4000–5500 Å, perhaps attributable to iron emission, have become more prominent relative to Mg I]. The apparent blueshift of the bright Mg I] λ4571 line is discussed in § 6.4.

Because of extensive blending of emission and absorption features, line identification in these spectra is quite difficult. The broad forest of lines between 4000–5500 Å is especially difficult to interpret quantitatively because of the many blended lines of iron and cobalt. More quantitative analysis of these spectra requires comparison with detailed spectrum synthesis models.

5. SPECTRUM SYNTHESIS RESULTS

In the following, we summarize the results of our synthetic spectrum analysis of the SN 1993J spectra. First we examine the effect on the spectrum of mixing in the ejecta. In this discussion, we highlight the way in which energy is absorbed and reemitted in the various composition zones. We then discuss in some detail the physical conditions present in the best-fit model and the evolution of this model during the first year.

5.1. *Energy Deposition in the Ejecta*

The rate of nonthermal energy deposition depends on the gamma-ray optical depth, the incident gamma-ray intensity, and the local ^{56}Co abundance. Where the ^{56}Co abundance is zero (i.e., outside the iron core), gamma-ray energy deposition is the primary energy source powering the emission, and the gamma-ray optical depth determines what fraction of the decay energy is absorbed. The distribution of the gamma-ray source determines the intensity of the gamma-ray flux at a given point. Where ^{56}Co is present, energy deposition from locally trapped positrons may provide a significant fraction of the nonthermal energy input. If the gamma-ray optical depth is small enough that locally trapped positrons dominate, the energy deposition rate will be insensitive to density changes resulting from mixing. In model 4H 47, gamma-ray absorption generally accounts for at least 80% of the nonthermal energy deposition in material from the iron core, while locally trapped positrons account for the remainder. Because of the lower density in model 3H 30, the gamma-ray optical depths are lower, making energy deposition by locally trapped positrons relatively more important. Mixing in 3H 30 may lower the density in the iron core material enough that gamma-ray deposition provides only 50% of the total energy input.

The optical emission from the iron core material is not only determined by locally absorbed ^{56}Co decay energy, but it also depends on the absorption of UV line photons from the oxygen shell and from the helium mantle. In material from the oxygen shell and helium mantle, the bulk of the nonthermal energy absorbed produces heating, and most of this heat is radiated in the ultraviolet by Mg II λ2803 and C II λ2326, respectively. When oxygen-rich material is mixed into the core, more gamma rays are absorbed in the oxygen-rich material and fewer are absorbed in the iron core material. The iron core material efficiently absorbs the increased UV radiation from the oxygen-rich material. These UV line photons are then degraded into optical photons, making the optical emission from the iron core material appear brighter than would be the case if positron and gamma-ray energy deposition were its only energy source. The absorption of this UV line radiation does not significantly affect the temperature or ionization state of the iron core material.

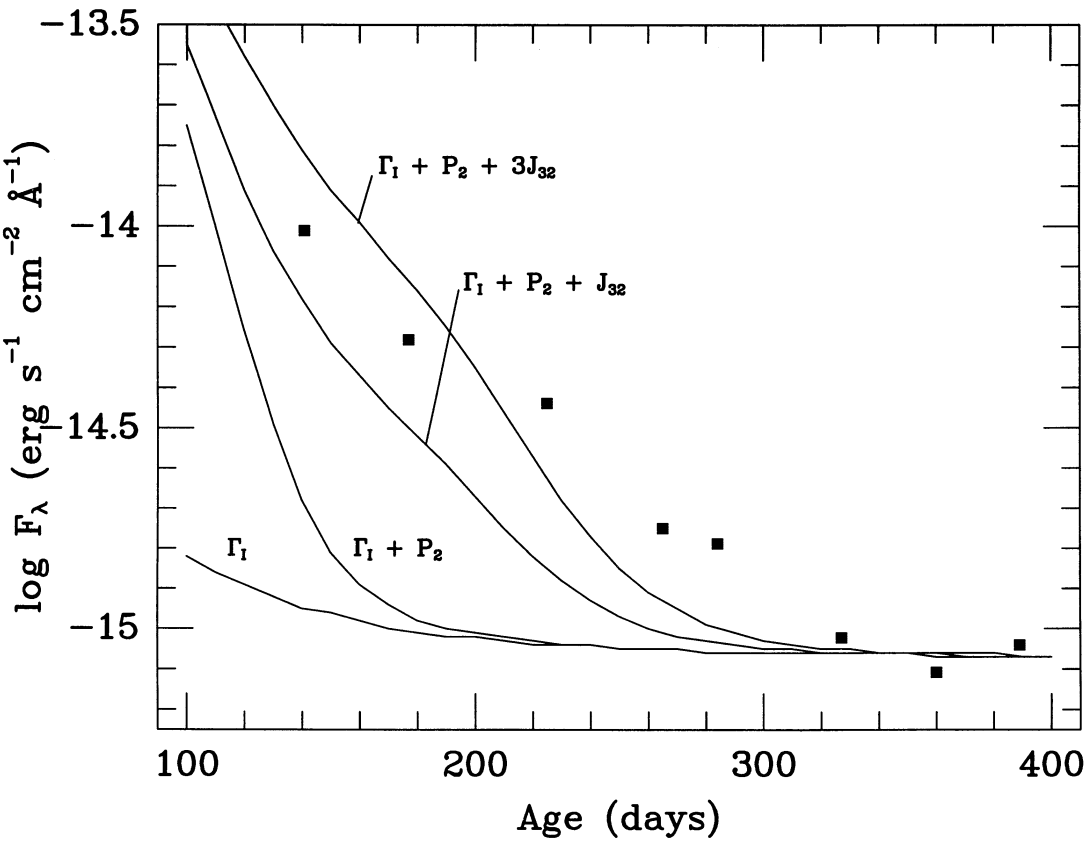

FIG. 3.—Evolution of the observed value of F_λ at Hα (*filled squares*) compared with various semianalytic estimates of the Hα flux. Filled squares represent the observed flux at 6563 Å; no attempt was made to separate out the Hα contribution from the blend of [O I] λλ6300, 6364 and Hα. Because the helium line widths indicate that the the brightest helium emission occurs within ~5000 km s^{-1} of line center, the contribution from He I λ6678 should be small. Similarly, the contribution from [O I] λλ6300, 6364 should be negligible. The constant Hα flux after ~300 days indicates circumstellar energy input. The curves are labeled according to which Hα production mechanisms contribute to the emission. Γ_I indicates recombination after nonthermal ionization, P_2 indicates recombination after photoionization in the Balmer continuum, and J_{32} indicates line scattering as discussed in the text with $J_{32} = 4 \times 10^{-8}$ ergs s^{-1} cm^{-2} Hz^{-1} sr^{-1} at 140 days. The factor $3J_{32}$ on the upper curve indicates that, for this curve, $J_{32} = 12 \times 10^{-8}$ ergs s^{-1} cm^{-2} Hz^{-1} sr^{-1} at 140 days.

5.2. *Unmixed versus Mixed Models*

In Figure 4, we compare the unmixed version of model 4H 47 with the observed spectrum at 140 days. In our computed spectrum, the O I emission lines [O I] λλ6300, 6364, [O I] λ5577, and O I λ7771 are overproduced, as are Mg I] λ4571, [Ca II] λ7307, and the Ca II IR triplet. Furthermore, the large computed value of the Ca II line ratio $I(7307)/I(8582)$ indicates that the temperature in the calcium-emitting region is too low. Aside from the strongest features, the mean flux level is reasonably well reproduced, except that the synthetic spectrum contains a number of narrow, relatively bright emission lines which are not present in the observed spectrum. Most of these narrow lines come from Fe I and Fe II at low velocities $\lesssim$2000 km s^{-1}. Overproduction of these lines indicates that, in the unmixed model, the iron core material absorbs too much energy; the absence of narrow iron lines in the observed spectrum is consistent with iron core material extending to velocities $\gtrsim$3000 km s^{-1}.

The unmixed version of model 3H 30 was less successful than model 4H 47 (Fig. 5). Over much of the observed range, the mean flux level in the synthetic spectrum was ~40% fainter than observed. While [Ca II] λ7307 is overproduced by about a factor of 4, the Ca II line ratio $I(7307)/I(8582)$ is much too large, and the other prominent lines of O I and Mg I are significantly underproduced. The optical emission was much fainter because the low-mass, high-velocity ejecta absorbed a much smaller fraction of the ^{56}Co decay energy than in 4H 47. Increasing the ^{56}Ni mass will not improve the fit because this will significantly increase the level of ionization.

To see the differences more clearly, we examine these two models in more detail. The gamma-ray optical depth of a shell of iron with uniform density is

$$\tau_\gamma \approx n\sigma_\gamma \Delta R = 0.2\left(\frac{M_{\rm Fe}}{0.1\ M_\odot}\right)\left(\frac{V_{\rm max}}{3000\ {\rm km\ s^{-1}}}\right)^{-2} t_{100}^{-2}\left(\frac{1-v}{1-v^3}\right), \quad (3)$$

where $v \equiv V_{\rm min}/V_{\rm max}$, $V_{\rm min}$ and $V_{\rm max}$ are the velocities at the inner and outer edges of the shell, $M_{\rm Fe}$ is the mass of the shell, and t_{100} is the age in units of 100 days. In obtaining this expression, we have written the number density in terms of the mass of iron contained in the shell and the velocity gradient across the shell. Both 3H 30 and 4H 47 have about the same mass of iron-rich core material: model 3H 30 has 0.1 $M_\odot$ of iron-rich core material, while model 4H 47 has 0.12 $M_\odot$. However, model 3H 30 expands more rapidly so that its iron core extends from $V_{\rm min} = 1000$ km s^{-1} to $V_{\rm max} = 2250$ km s^{-1}, with gamma-ray optical depth $\tau_\gamma \approx 0.1$. In contrast, the iron core in model 4H 47 lies between $V_{\rm min} = 1000$ km s^{-1} and $V_{\rm max} = 1500$ km s^{-1} and has a larger gamma-ray optical depth

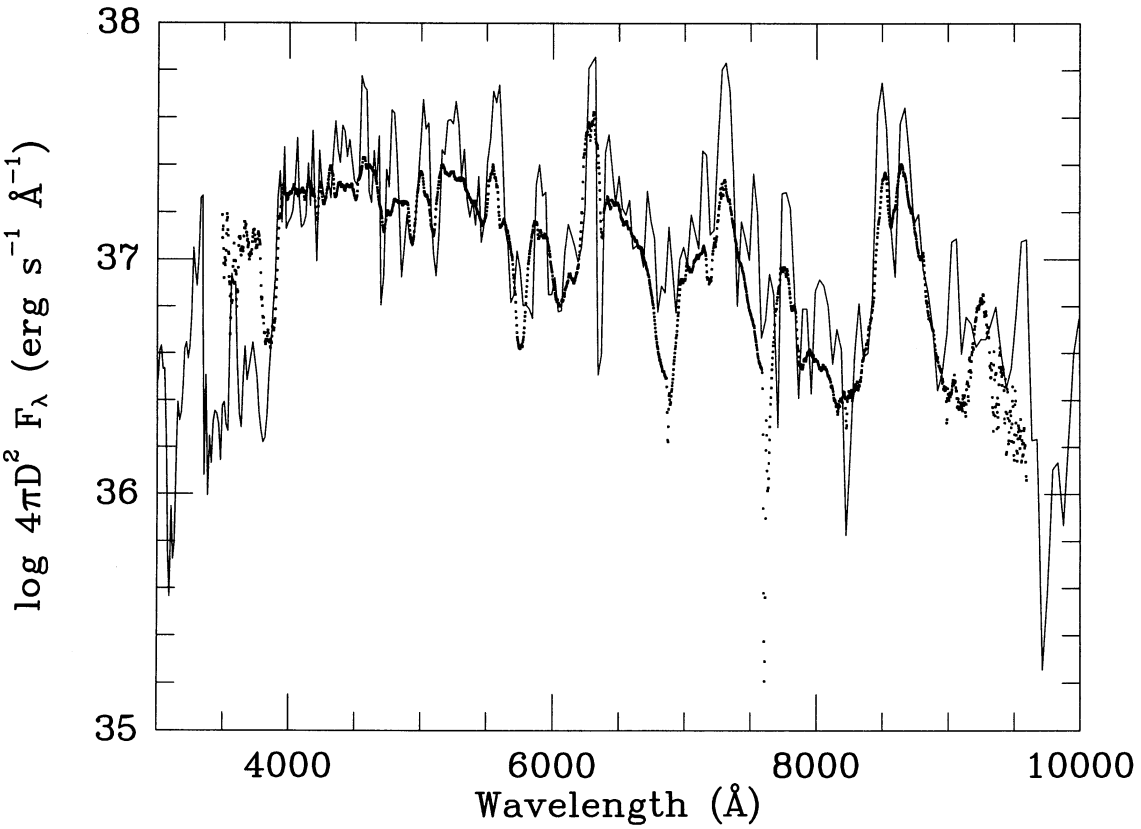

FIG. 4.—Synthetic spectrum for model 4H 47 (unmixed) at 140 days, compared with the observed spectrum (points). Without mixing, the O I emission lines [O I] λλ6300, 6364, [O I] λ5577, and O I λ7771 are overproduced, as are Mg I] λ4571, [Ca II] λ7307, and the Ca II IR triplet. The large computed value of the Ca II line ratio $I(7307)/I(8582)$ indicates that the temperature in the calcium-emitting region is too low. Aside from the strongest features, the mean flux level is reasonably well reproduced except that the synthetic spectrum contains a number of narrow, relatively bright emission lines which are not present in the observed spectrum.

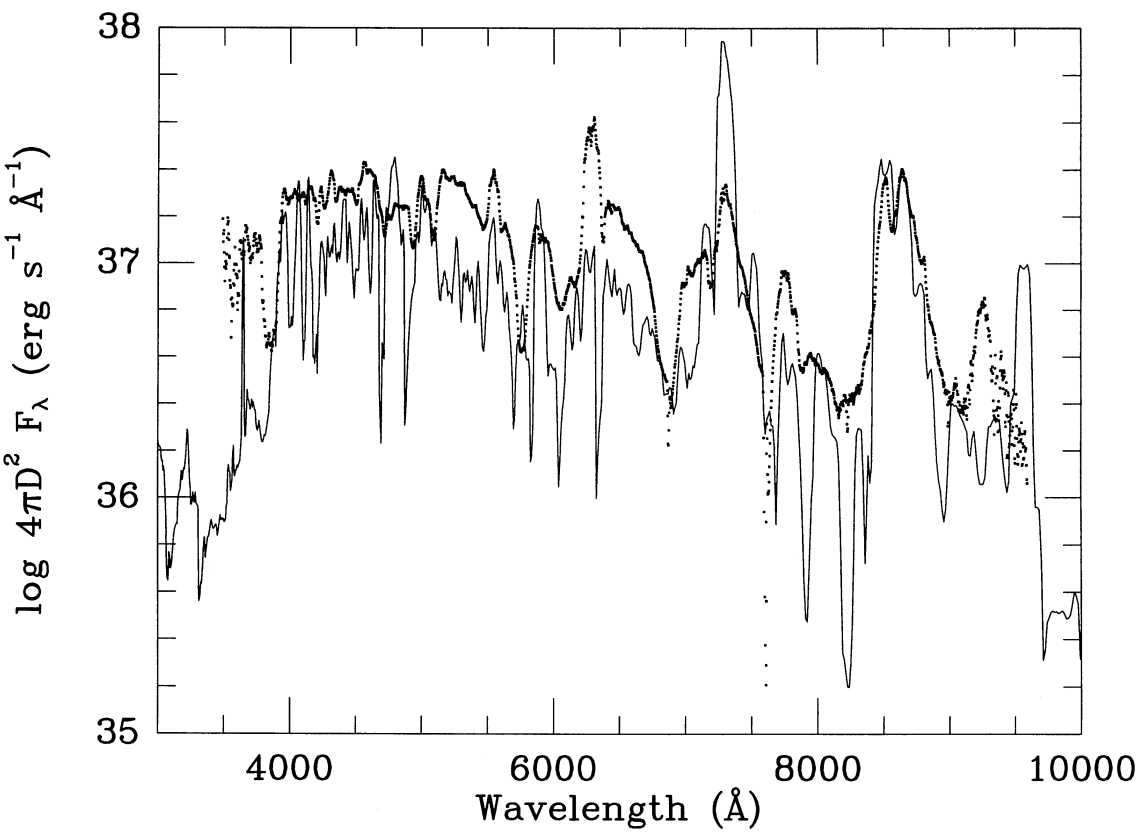

FIG. 5.—Synthetic spectrum for model 3H 30 (unmixed) at 140 days, compared with the observed spectrum (*points*). The optical emission is much fainter than in model 4H 47 because the low-mass, high-velocity ejecta in 3H 30 absorbed a much smaller fraction of the ^{56}Co decay energy. In particular, the oxygen emission is underproduced by a factor of 3.

$\tau_\gamma = 0.22$. In 3H 30, the concentration of ^{56}Co is roughly twice as high as in 4H 47, while the core helium abundance resulting from the alpha-rich freezeout is much smaller. This means that positron deposition is proportionally more important in 3H 30, so that the energy absorbed in the core material is less sensitive to mixing. Because of the lower gamma-ray optical depth of its core material, the iron emission in 3H 30 is weaker than in 4H 47 by a factor ~ 2. Similarly, because of its low oxygen mass and low helium mass, 3H 30 significantly underproduces emission lines from these species. The O I recombination lines at 7771 Å and 9264 Å are underproduced by about a factor of 3, as are the collisionally excited features at 6300 Å and 5577 Å. The helium features He I λ5876 and He I λ7065 are underproduced by similar factors.

The overproduction of narrow iron lines in model 4H 47 can be corrected by reducing the amount of energy absorbed in the iron core and spreading the iron over a broader velocity range. Such macroscopic mixing of the core material has been discussed extensively in relation to SN 1987A and other core collapse supernovae (Herant & Benz 1991; Fryxell, Arnett, & Müller 1991; Shigeyama & Nomoto 1990; Shibazaki & Ebisuzaki 1988; and references therein). Light-curve calculations by Shigeyama et al. (1994) also indicate that outward mixing of ^{56}Ni may have occurred in SN 1993J. Recent two-dimensional models specifically computed by Iwamoto (1994) are reported in Nomoto, Iwamoto, & Suzuki (1995). These models display extensive mixing at the Fe-Ca/O interface with iron mixed out to ~ 4000 km s^{-1} and oxygen mixed inward to relatively low velocities. Having a smaller envelope mass than the 4H 47 model, the amount of mixing at the H/He interface is reduced.

Our macroscopic mixing of the ejecta of model 4H 47 involved the inner 0.85 $M_\odot$ of material out to 3000 km s^{-1}, including the iron core and most of the oxygen shell. Material rich in ^{56}Co was mixed through the inner 0.6 $M_\odot$ of material, increasing the maximum expansion velocity of the iron core material from 1500 km s^{-1} to 3000 km s^{-1}. This mixing reduced the gamma-ray optical depth of the iron core material by about a factor of 2, from $\tau_\gamma \approx 0.22$ to $\tau_\gamma \approx 0.11$, reducing the gamma-ray energy deposited in the core material by a similar factor (Fig. 6). The total nonthermal energy deposited in the iron core material fell by 67% as a result of the decrease in gamma-ray optical depth and the decreased gamma-ray intensity. However, this large decrease in energy input was compensated by a corresponding decrease in the cooling rate at the lower density, so that the temperature and level of ionization decreased only slightly. The net decrease in optical brightness was smaller than might have been expected because absorption of UV line radiation from the oxygen-rich material helped offset the decrease in locally powered iron and cobalt optical emission. With broader line profiles, the iron and cobalt features throughout the spectrum were more strongly blended, improving the fit to the observed spectrum. Some iron lines

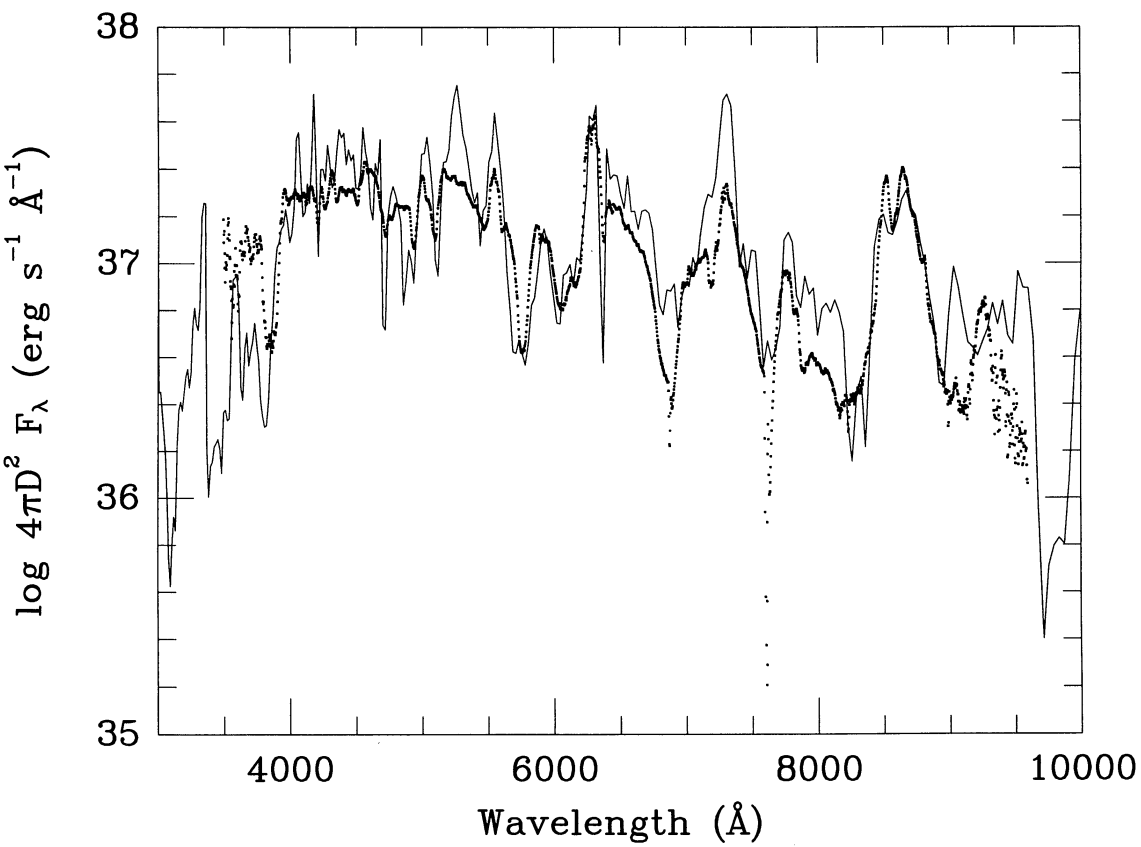

FIG. 6.—Synthetic spectrum for model 4H 47 (mixed) at 140 days, compared with the observed spectrum (*points*). Macroscopic mixing reduced the total nonthermal energy deposited in the iron core material by 67%. The net decrease in optical brightness is smaller than might have been expected because absorption of UV line radiation from the oxygen-rich material helped offset the decrease in locally powered iron and cobalt optical emission. With broader line profiles, the iron and cobalt features throughout the spectrum are more strongly blended, improving the fit to the observed spectrum. The O I emission lines are $\sim 30\%$ weaker, mainly because of a shift toward higher ionization caused by the decrease in density as a result of mixing.

were still overproduced, however. In particular, the Fe I emission lines near 8000 Å and the Fe I features at 9000 Å and 9571 Å were overproduced by about a factor of 2. The O I emission lines were ~30% weaker, mainly owing to a shift toward higher ionization caused by the decrease in density, from $n = 3.7 \times 10^8$ cm^{-3} in the unmixed model, to $n = 2.5 \times 10^8$ cm^{-3} in the mixed model. The increase in ionization also produces a better fit to the Mg I] λ4571 line (§ 6.4).

Although the unmixed version of model 3H 30 and the mixed version of 4H 47 contain about the same mass of iron core material with the same gamma-ray optical depth, the optical spectrum produced by the mixed version of 4H 47 is significantly brighter. This is mainly because 4H 47 has a more massive oxygen shell and a higher mean density. In 4H 47, the Mg II λ2803 line, responsible for much of the cooling of the oxygen-rich material, is absorbed in the iron core material which then reradiates the energy in the optical.

Figure 7 shows the synthetic spectrum based on the mixed version of model 3H 30. In this model, mixing involved the iron core and the oxygen shell, or about 0.45 $M_\odot$ of ejecta below ~4000 km s^{-1}. Because iron core material was mixed to higher velocities, the iron lines are much broader and, in that sense, they agree better with the observed spectrum. As expected, mixing did not increase the optical luminosity, so the mean flux level remains too low. Despite increased gamma-ray energy deposition, the O I emission in particular remains significantly weaker than in the observed spectrum. Because it was mixed inward, calcium was exposed to a somewhat larger gamma-ray flux, increasing its temperature from ~5000 K, to ~6000 K and increasing the level of ionization as well. The temperature increase improved the fit to the observed Ca II line ratio $I(7307)/I(8582)$, but the increased ionization reduced the total emitting mass of Ca II so that the total Ca II emission is roughly a factor of 2 fainter than observed.

The main conclusion from the mixed models is that, independent of the level of mixing, model 3H 30 significantly underproduces most features in the optical spectrum. In particular, the oxygen lines are underproduced by about a factor of 3, indicating that the oxygen mass in SN 1993J is considerably larger than the 0.24 $M_\odot$ of oxygen produced in model 3H 30. In contrast, the observed oxygen features are well represented by the mixed version of model 4H 47 with ~0.5 $M_\odot$ of oxygen. Aside from its overproduction of several iron lines, probably because of poor atomic data, and the poor fit to the Ca II line ratio $I(7307)/I(8582)$, the mixed version of model 4H 47 provides a reasonably good fit to the observed optical spectrum. The latter may be a result of excessive Co II cooling caused by inaccurate atomic data. Experiments in which cobalt cooling was excluded considerably improved the fit to the Ca II line ratio. This model should therefore closely approximate the physical conditions in the nebula; in the next few paragraphs we describe the physical structure of this model in greater detail.

5.3. *Physical Conditions*

We begin our discussion of the physical conditions in SN 1993J by contrasting the Type IIb SN 1993J with the well-studied Type II SN 1987A. The primary differences arise from

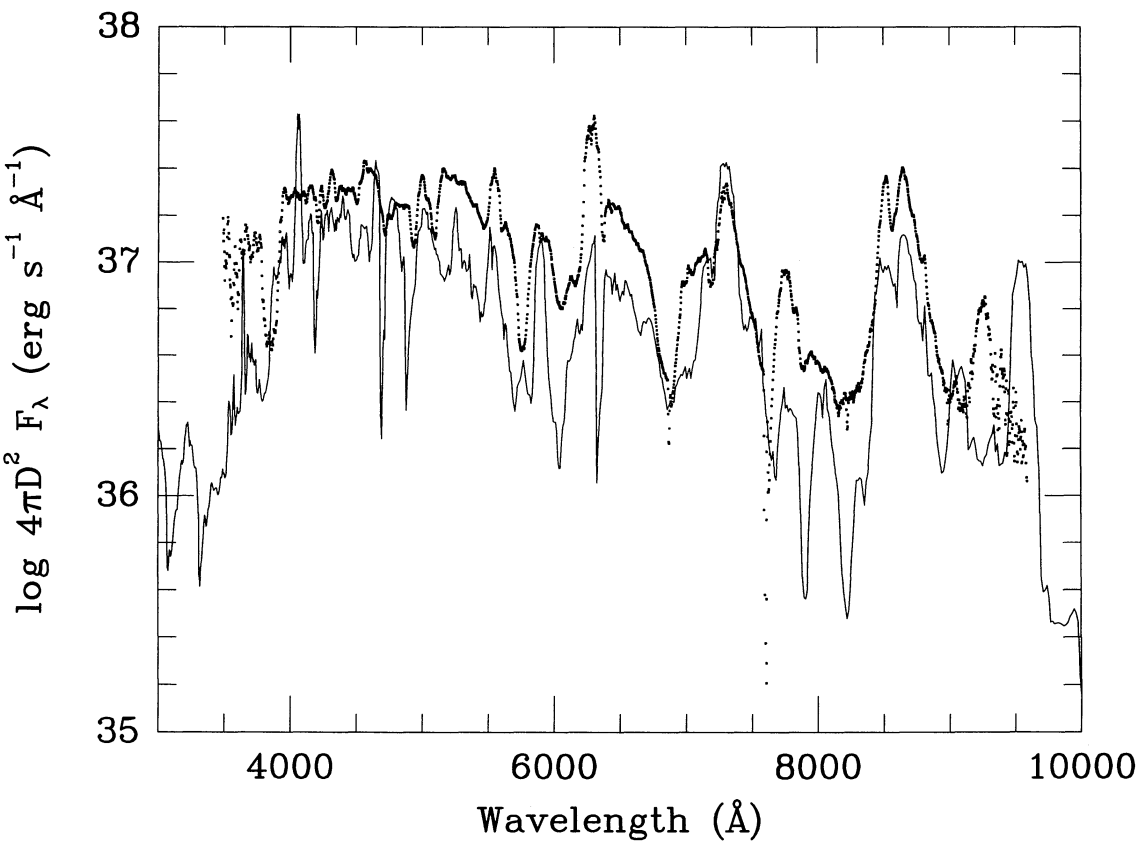

FIG. 7.—Synthetic spectrum for model 3H 30 (mixed) at 140 days, compared with the observed spectrum (*points*). As expected, mixing did not increase the optical luminosity; the mean flux level remains too low. In particular, the O I and He I emission remain significantly weaker than in the observed spectrum.

the large difference in the ejecta mass in the two cases. SN 1987A had a similar total kinetic energy, but because the ejecta mass was several times larger, SN 1987A expanded more slowly and was much denser. In SN 1987A at age 150 days, the density was $n \gtrsim 10^{10}$ cm^{-3}, making the ejecta much cooler and less highly ionized than in SN 1993J, which had a density $n \lesssim 5 \times 10^8$ cm^{-3} at this epoch (Fransson 1994; Kozma & Fransson 1991). In the high-density case, a larger fraction of the energy deposited by ^{56}Co gamma rays goes into ionization and direct excitation of resonance transitions, while a smaller fraction goes into heating the electron gas. With its lower density, most of the nonthermal energy deposition in SN 1993J goes into heating, with $\lesssim$15% producing ionizations and, except in the H/He envelope, a negligible fraction going into direct excitation.

In our best-fit mixed model for SN 1993J (4H 47), the inner 0.85 $M_\odot$ of ejecta inside $\sim$3000 km s^{-1} were mixed, distributing ^{56}Co through the inner 0.6 $M_\odot$ of ejecta. In addition, the H/He envelope was shifted into the velocity range 8500–10,000 km s^{-1} to improve the fit to the position and width of the observed Hα absorption feature (§ 6.1.5). The H/He envelope was displaced outward by adding $\sim$0.1 $M_\odot$ of material to the He mantle.

5.3.1. *140 Days*

The physical conditions at age 140 days are summarized in Table 1. In this mixed model, the mass density in the oxygen core was uniform, with $\rho \approx 7.3 \times 10^{-15}$ g cm^{-3}. Oxygen-rich zones alternated with zones rich in iron and cobalt. Approximately 85% of the nonthermal energy deposited in this oxygen-rich material produced heating in the free electron gas. In the iron core material, the composition varied with the relative concentration of helium from alpha-rich freezeout, and silicon and sulfur from explosive oxygen burning. The oxygen-rich material had a smaller gamma-ray absorption cross section per atom than the iron core material, but the iron core material cooled more efficiently. As a result, the iron-rich zones were typically much cooler than the oxygen-rich zones. Approximately 80% of the nonthermal energy deposition in the iron core material went into heating. The Fe/Si zones produced the bulk of the [Ca II] λ7307 and [Ca II] triplet emission from the supernova. Because the [Ca II] triplet was underproduced relative to [Ca II] λ7307, we inferred that this temperature was somewhat lower than the actual temperature in the Fe/Si-rich material.

In the helium mantle, most ($\sim$70%) of the gamma-ray energy absorbed produced heating in the electron gas, while $\sim$25% produced ionization and $\sim$5% went into direct excitation. Most of the nonthermal ionization energy ionized He I, and $\sim$25% of subsequent recombinations went to He I singlet states, ultimately producing two-photon emission. He I two-photon emission, also powered by direct nonthermal excitation, then ionized most of the trace neutral ions, C I in particular. Although the carbon abundance was only $\sim$1% by number, C II] λ2326 emission provided more than 80% of the cooling and, through photoionization of He I, affected the ionization balance as well. Collisionally excited C II] λ2326 emission photoionized He I from the $2s\,^3S$ state with relatively high efficiency because the large population of this metastable He I state gave it a continuum optical depth $\tau \approx 0.2$. Because this mechanism tapped the large fraction of nonthermal energy going into heat, ionization of helium was dominated by C II] λ2326, with nonthermal ionization contributing only about 30% of its ionization rate. The overall ionization balance was somewhat temperature sensitive because the electron temperature was low compared to the excitation temperature of C II] λ2326.

Approximately 60% of the nonthermal energy deposition in the H/He envelope produced heating, while 25% went into ionization and 15% to direct excitation. Excitation of the $n = 2$ state of H I was dominated by recombination and thermal and nonthermal excitation from $n = 1$. Interestingly, the most important mechanism for populating $n = 3$ and producing the observed Hα emission between $\sim$100–300 days was absorption of line photons in the Balmer series, in particular, absorption in Hα of redshifted [O I] λ6364 photons. The contribution to $n = 3$ from recombination, direct nonthermal excitation from $n = 1$, and collisional excitation from $n = 2$ was more than an order of magnitude smaller. At $\sim$140 days, Balmer continuum photoionization of hydrogen was comparable to the nonthermal ionization rate. Roughly half the Balmer continuum radiation field came from local Mg II λ2803 and two-

TABLE 1

PHYSICAL CONDITIONS AT 140 DAYS

Composition	V (km s^{-1})	n (10^8 cm^{-3})	T (K)	x_e	Coolants
Fe/He	1000–4000	1.0–2.5	4000	0.6	Co II (45%) Fe II (35%) Fe I (10%)
Fe/Si	1000–4000	1.0	3800	1.0	Ca II (40%) Fe I (40%) Co II (15%)
Oxygen	1000–4000	1.0–2.5	6300	0.75	Mg II $\lambda\lambda$2803 (50%) Mg I] λ4571 (20%) [O I] $\lambda\lambda$6300, 6364 (10%)
C/O	3000–3300	2.0–3.0	5800	0.34	C I (60%) Mg II $\lambda\lambda$2803 (19%) [O I] $\lambda\lambda$6300, 6364 (10%)
Helium	4000–8500	0.5–3.0	7500–8500	0.2	C II] λ2326 (80%)
Envelope	8500–10,000	0.5	8500	0.1	Mg II $\lambda\lambda$2803 (40%) H I λ1216 (35%) Fe II (25%)

photon emission and half came from UV photons from the interior of the nebula, mainly Mg I λ2853, Mg II λλ2803, C II] λ2326, and ~3000 Å emission from the recombination cascade of neutral and singly ionized iron and cobalt. Trace neutral elements were strongly photoionized by two-photon emission.

5.3.2. *284 Days*

In the oxygen-rich material at this epoch, the lower density slowed recombination, favoring increased ionization of magnesium. As a result, the Mg I abundance was lower, with cooling still dominated by Mg II λλ2803. The temperature decreased to $T = 4600$ K, with ~60% of the cooling attributable to Mg II and the rest to O I (~25 %) and Mg I (~5 %). O I cooling increased because the lower temperature favored lower excitation lines. The electron fraction was $x_e \approx 0.6$, so that the nonthermal energy deposition was distributed in much the same way as at 140 days. In the C/O region, the temperature decreased to $T = 4750$ K, with $x_e \approx 0.4$. At this lower temperature, the balance of cooling shifted toward lines with lower excitation temperature, so that [O I] λλ6300, 6364 cooling increased at the expense of Mg II λλ2803. Most of the cooling was caused by [C I] (~50%), with the remainder attributable to O I (~34%) and Mg II (~5%).

Because the cobalt abundance decreased as a result of radioactive decay, iron cooling became more important in the iron core. In the Fe/He regions, Fe II accounted for ~70 % of the cooling compared to ~24% for Co II, while in the Fe/Si regions, cooling was dominated by Fe II (~30%), Ca II (~50%), and Co II (~16%). The importance of cobalt as a coolant may have been overestimated, however, because of errors in the uncertain atomic data. The lower density favored higher ionization so that $x_e \approx 1.2$, while the temperature decreased to $T = 3500$ K.

Aside from the decrease in density, the physical conditions in the He mantle and H/He envelope were much the same as at 140 days. At the lower density, Balmer continuum photoionization of H I was much less efficient, as was scattering of [O I] λ6364. Models neglecting circumstellar input tended to underproduce the observed Hα feature by about a factor of 2 (Fig. 8). However, interpreting the observed Hα luminosity as a function of time (Fig. 3) with a simple model in which a constant fraction of Hα emission was caused by circumstellar input, one expects that roughly 50% of the observed Hα emission was caused by the circumstellar interaction at this epoch.

6. DISCUSSION OF INDIVIDUAL ELEMENTS

Line identifications based on a synthetic spectrum calculation at age 140 days are given in Figure 2. Most agree with the identifications given by Lewis et al. (1994), although in the case of the oxygen and magnesium lines, our interpretation is significantly different. In this section, we discuss constraints on the masses of hydrogen, helium, and oxygen and outline the uncertainties associated with the computed strengths of other prominent spectral features.

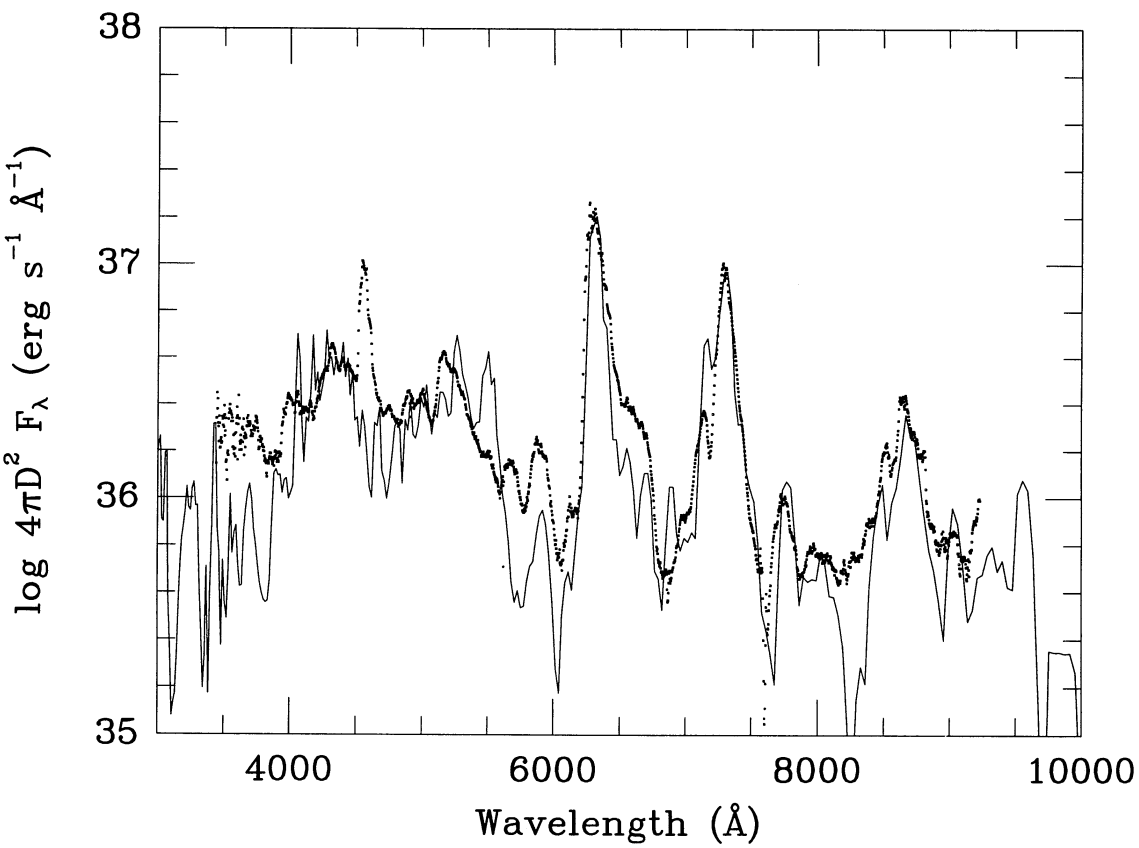

FIG. 8.—Synthetic spectrum for model 4H 47 (mixed) at 284 days, compared with the observed spectrum (*points*). Hα is underproduced because circumstellar energy input is an important energy source for the Hα luminosity but was not included in this calculation. Because of the relatively high degree of ionization in the oxygen-rich material, the Mg I] λ4571 line is underproduced in this calculation.

6.1. *Constraints on the Hydrogen Mass*

The total hydrogen mass and its distribution in velocity can be constrained in several ways. The simplest constraint, based on energetics, limits the mass of material at high velocity ($\gtrsim 10^4$ km s^{-1}), for a given explosion kinetic energy. The kinetic energy of a constant velocity, pure hydrogen shell of mass $M_{\rm env}$ solar masses is $E_K = 10^{51} M_{\rm env} v_4^2$ ergs, where v_4 is the expansion velocity in units of 10^4 km s^{-1}. If the total available kinetic energy is of order 10^{51}ergs, the mass at high velocity ($\gtrsim 10^4$ km s^{-1}) must be $\ll 1\ M_\odot$. However, this constraint does not rule out a significant mass of hydrogen at a relatively low velocity of order a few thousand km s^{-1}.

More direct constraints come from consideration of the Hα emissivity and line blending effects. Because hydrogen mixed into the low-velocity interior of the ejecta is compressed, increasing its gamma-ray optical depth, and because it is exposed to a relatively intense gamma-ray and Balmer continuum flux, it produces strong Hα emission. Therefore, the observed Hα flux constrains the mass of hydrogen at low velocity ($\lesssim$5000 km s^{-1}). In the intermediate-velocity range, the hydrogen mass is constrained by the observed line blending effects as well as the observed Hα luminosity. The bright Hα emission observed after $\sim$300 days, probably as a result of energy input from circumstellar X-rays, may provide an additional constraint on the hydrogen mass (Fransson & Houck 1995). In the next few sections, we discuss these spectrum constraints in turn. First we discuss the most important mechanisms for producing the observed Hα emission, then we discuss the behavior of the Hα luminosity and optical depth as a function of time.

6.1.1. *Mechanisms Producing* Hα *Emission*

Because the temperature in the H/He envelope is low, $T \lesssim 9000$ K, collisional excitation and collisional ionization are inefficient compared to recombination. Hα is produced mainly through recombination after nonthermal ionization and photoionization from $n = 2$ and through absorption and scattering of Balmer photons. In the following, we will develop approximate analytic expressions for the nonthermal and photoionization rates and for the mean intensity of the incident radiation field being absorbed in the Balmer series. The ultimate energy source for the emission is radioactive decay of ^{56}Co; the total rate of energy release from ^{56}Co decay is $L_\gamma = 1.27 \times 10^{43} M_{\rm Ni} e^{-t/111\ {\rm days}}$ ergs s^{-1}, where $M_{\rm Ni}$ is the ^{56}Ni mass in solar masses. We consider a spherically symmetric model in which the H/He envelope occupies a shell. The core of material inside this shell has radius $R_c = V_c t$ and gamma-ray optical depth $\tau_{\gamma,c} \approx 0.09 Z n_8 v_4 t_{100}$, where v_4 is the core expansion velocity V_c in units of 10^4 km s^{-1} and n_8 is the number density in units of 10^8 cm^{-3}.

Direct nonthermal energy deposition in the H/He envelope produces ionization, heating, and direct excitation. The rate of nonthermal ionization of neutral hydrogen is expressed in terms of an effective ionization potential $\chi_{\rm eff} = 13.6\ {\rm eV}/f_{\rm ion}$, where $f_{\rm ion}$ is the fraction of nonthermal energy ionizing neutral hydrogen (Kozma & Fransson 1991). The nonthermal ionization rate from $n = 1$ is then

$$\Gamma_I = \frac{L_\gamma e^{-\tau_{\gamma,c}}}{4\pi R_c^2} \frac{\sigma_\gamma}{\chi_{\rm eff}} = 1.06 \times 10^{-6} e^{-\tau_{\gamma,c}} \left(\frac{\chi_{\rm eff}}{60\ {\rm eV}}\right)^{-1} v_4^{-2} t_{100}^{-2} e^{-t/111^{\rm d}}\ {\rm s}^{-1} . \quad (4)$$

A fraction $f_{\rm H}$ of nonthermal energy deposited in the H/He envelope produces heating in the free electron gas with an additional fraction f_{13} producing direct excitations to $n = 3$. The direct nonthermal excitation rates to $n = 2$ and $n = 3$ are then Γ_{12} and Γ_{13}, respectively. The $n = 2$ excitation rate may be written $\Gamma_{12} = \Gamma_I(\chi_{\rm eff} f_{12}/\epsilon_{12})$, where f_{12} is the fraction of nonthermal energy-producing excitations to $n = 2$ and ϵ_{12} is the Lyα photon energy. A similar expression can be written for Γ_{13}.

The photoionizing radiation field in the Balmer continuum originates both from local emission in the H/He envelope and as a result of gamma-ray energy deposition in the interior of the nebula depends. A fraction, f_{2c}, of the nonthermal energy deposited in the interior of the nebula is converted into photons capable of ionizing hydrogen from $n = 2$. The Balmer continuum ionization rate per atom attributable to these photons is approximately

$$P_2 = f_{2c} \frac{L_\gamma (1 - e^{-\tau_{\gamma,P}})}{4\pi R_c^2} \frac{\sigma_{\rm B}}{\chi_{\rm B}} = 2.8 \times 10^3 f_{2c} (1 - e^{-\tau_{\gamma,P}}) \left(\frac{h\nu}{\chi_{\rm B}}\right)^{-2.9} v_4^{-2} t_{100}^{-2} e^{-t/111^{\rm d}}\ {\rm s}^{-1} , \quad (5)$$

where $\sigma_{\rm B} = 1.5 \times 10^{-17} (h\nu/\chi_{\rm B})^{-2.9}$ cm^2 is the photoionization cross section from $n = 2$, $\chi_{\rm B}$ is the Balmer ionization threshold, and $h\nu$ is the ionizing photon energy. The gamma-ray optical depth $\tau_{\gamma,P}$ refers to the size of the region which contributes to this Balmer continuum radiation field; for a H/He shell at low velocity, this region may include material outside the shell itself. Kozma & Fransson (1991) found $f_{2c} = 0.2$–0.3.

While the ionization balance is determined by these two ionization processes, most of the observed Hα flux up to age 300 days is produced as a result of line blending effects. Line blending is especially important because of the large velocity gradient in the expanding nebula; the redshift between two widely separated points in the nebula may be comparable to the separation between two spectral lines, enabling one line to shift into resonance with another. A particularly important case is that in which redshifted [O I] $\lambda\lambda$6300, 6364 photons can come into resonance with Hα (Fig. 9). Absorption of [O I] λ6364 by Hα is essentially a scattering process which produces an Hα emission feature. Absorption of line photons by other Balmer series transitions should also lead to the emission of an Hα photon plus one or more infrared photons.

Assuming that [O I] λ6364 is the primary source of photons, we can use the observed spectrum to estimate J_{32}, the mean intensity incident in Hα. At 140 days, the unabsorbed intensity of [O I] λ6364 is $F_\lambda \approx 10^{-14}$ ergs s^{-1} cm^{-2} Hz^{-1} sr^{-1}; in the H/He envelope, the mean intensity resulting from this line is then

$$J_{32} = (\lambda^2/c)(4\pi)^{-1}(D/R)^2 F_\lambda \approx 10^{-8}\ {\rm ergs\ s^{-1}\ cm^{-2}\ Hz^{-1}\ sr^{-1}} . \quad (6)$$

A similar intensity from various iron lines is incident at Hβ, so that the corresponding quantity $J_{42} \approx 0.6 \times 10^{-8}$ ergs s^{-1} cm^{-2} Hz^{-1} sr^{-1}. Using an effective value of J_{32} to account for the flux incident in all Balmer lines, we estimate that $J_{32} \gtrsim 2 \times 10^{-8}$ at 140 days. In the simplest approximation, this quantity has the same time dependence as P_2 since both arise from nonthermal energy deposition in the interior of the nebula.

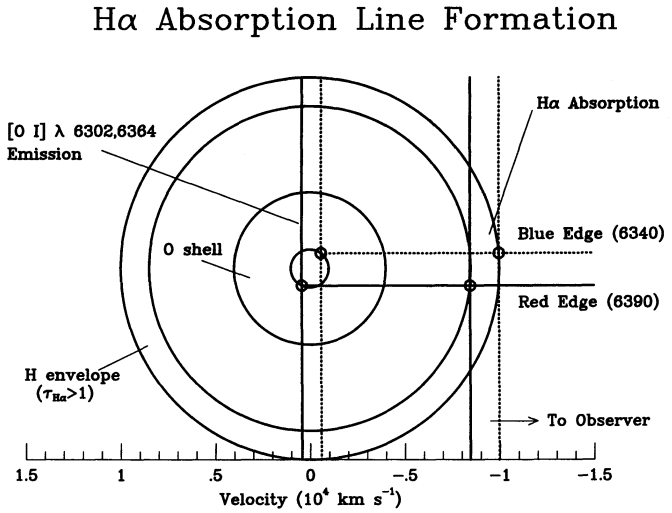

FIG. 9.—Geometry of the Hα –[O I] λλ6300, 6364 blend showing the location of the oxygen shell (1000–4000 km s^{-1}) and the H/He envelope (8500–10,000 km s^{-1}) with a velocity scale showing relative velocities along the line of sight. [O I] λλ6300, 6364 emission along the solid vertical line crossing the oxygen shell is Doppler-shifted into resonance with Hα along the solid vertical line crossing the H/He envelope. Scattering of [O I] λλ6300, 6364 by Hα produces the redward edge of the observed Hα absorption feature at 6390 Å. Similarly, the vertical dotted lines indicate the resonance planes which produce the blueward edge of the absorption feature at 6340 Å. It is apparent from the figure that scattering by Hα produces an absorption feature ~1000 km s^{-1} wide, roughly centered on the [O I] λ6364 line.

Therefore, we will use the expression

$$J_{32} = J_0(1 - e^{-\tau_{\gamma,c}})v_4^{-2}t_{100}^{-2}e^{-t/111\ \mathrm{days}}$$
$$\mathrm{ergs\ s^{-1}\ cm^{-2}\ Hz^{-1}\ sr^{-1}}, \quad (7)$$

with the constant coefficient J_0 fixing the scale of J_{32}. Although the [O I] λ6302 brightness decays somewhat more slowly between 140–250 days, this expression provides a rough estimate of the incident intensity.

6.1.2. *Simplified Model for* Hα *Emission*

To estimate the Hα optical depth and the Hα luminosity as a function of time, we treat hydrogen as a three-level atom plus continuum. We include contributions from photon absorption in Balmer lines, direct nonthermal excitation of $n = 2$ and $n = 3$, recombination, photoionization from $n = 2$, and nonthermal ionization from $n = 1$. We neglect thermal electron collisions. The effective recombination rate to $n = 3$ is $\alpha_C \equiv \sum_{k=3}^{\infty} \alpha_k$, while the total effective recombination rate is $\alpha_t \equiv \alpha_C + \alpha_2 e^{-\tau_B}$, where τ_B is the optical depth in the Balmer continuum. Depending on the optical depth in the Balmer continuum, $\alpha_C \leq \alpha_t$. With these definitions, the equations governing statistical equilibrium, ionization balance, and particle number conservation in a pure hydrogen gas may be written

$$n_3 A_{32}\beta_{32}\left(1 - \frac{J_{32}}{S_{32}}\right) = n_1\Gamma_{13} + n_e n_+ \alpha_C\,, \quad (8a)$$

$$n_2(A_{2\gamma} + A_{21}\beta_{21} + P_2) = n_1\Gamma_{12} + n_e n_+ \alpha_2 + n_3 A_{32}\beta_{32}\left(1 - \frac{J_{32}}{S_{32}}\right), \quad (8b)$$

$$n_e n_+ \alpha_t = n_1\Gamma_I + n_2 P_2\,, \quad (8c)$$

$$n = n_1 + n_2 + n_3 + n_+\,, \quad (8d)$$

where J_{32} is the mean intensity absorbed in Hα and S_{32} is the Hα source function. The two-photon transition probability is $A_{2\gamma}$, A_{21} is the Lyα transition probability, and $\beta_{21} \equiv (1 - e^{-\tau_{21}})/\tau_{21}$ is the Sobolev escape probability for Lyα.

6.1.3. *Hα Emission from Low-Velocity Hydrogen*

Hydrogen envelope material may be mixed to low velocities, similar to SN 1987A (Fryxell et al. 1991; Herant & Benz 1992). Here we discuss constraints on this mass from the Hα line. In hydrogen at low velocity, scattering of redshifted [O I] λ6364 emission is unimportant because the velocity relative to the oxygen-emitting material is insufficient to shift the two lines into resonance. Instead, low-velocity hydrogen produces Hα emission primarily through recombination after nonthermal ionization from $n = 1$ and photoionization in the Balmer continuum. Because the intensity of the ionizing radiation field increases roughly $\propto V^{-2}$, the Balmer continuum photoionization rate is more than an order of magnitude larger for hydrogen at low velocities ($\lesssim$2000 km s^{-1}) than for the hydrogen envelope at ~9000 km s^{-1}.

Solving equations (8a)–(8d) for the case of a 0.1 $M_\odot$ pure hydrogen shell between 2000–4400 km s^{-1} and with $J_{32} = 0$ (no scattering of [O I]), we find that the ionization balance is dominated by photoionization in the Balmer continuum. At 140 days, this analytic model gives $x_e = 0.7$ and $F_\lambda \approx 1.8 \times 10^{-14}$ ergs s^{-1} cm^{-2} $Å^{-1}$, about a factor of 2 larger than the observed flux at Hα . This indicates that $\gtrsim$0.1 $M_\odot$ of hydrogen at $\lesssim$5000 km s^{-1} should be clearly detectable.

Detailed synthetic spectrum calculations are consistent with this result, indicating that the presence of 0.1 $M_\odot$ hydrogen below 3000 km s^{-1} results in a bright, relatively narrow Hα emission line which was not observed. A model with 0.1 $M_\odot$ of hydrogen envelope material between 1900–2400 km s^{-1} with density 1.5×10^9 cm^{-3} produced a bright Hα emission line 4800 km s^{-1} wide, with peak flux $F_\lambda = 1.4 \times 10^{-14}$ ergs s^{-1} cm^{-2} $Å^{-1}$, significantly larger than the observed flux at Hα this epoch. About 50% of the input to $n = 3$ was collisional excitation from $n = 2$, and 45% was caused by recombination. At threshold, the Balmer continuum optical depth across the zone was $\tau_B = 4.2$; ionization of hydrogen was dominated by photoionization from $n = 2$. Direct nonthermal excitation and recombinations after nonthermal ionization contributed only ~10% of the population of $n = 3$. We conclude that the hydrogen mass at low velocities is strongly constrained to $\lesssim$0.1 $M_\odot$ by the observational limits on the Hα luminosity between 100–250 days.

6.1.4. Hα *Emission from High-Velocity Hydrogen*

Pure recombination is unlikely to explain the observed Hα luminosity. If every recombination to $n \geq 3$ produces an Hα photon, the Hα luminosity should be

$$L_{H\alpha} = x_e^2 \alpha_C h\nu_{32} n\left(\frac{M_H}{m_p}\right) = 2.4 \times 10^{38} n_8 \left(\frac{x_e}{0.1}\right)^2 \left(\frac{M_H}{0.3\ M_\odot}\right) \mathrm{ergs\ s^{-1}}\,, \quad (9)$$

where M_H is the mass of hydrogen. For an envelope density $n_8 = 0.5$ and $x_e = 0.1$, this corresponds to a flux of only $F_\lambda \approx 2 \times 10^{-16}$ ergs s^{-1} cm^{-2} $Å^{-1}$, much smaller than the observed value at 140 days. At 225 days, the discrepancy is even larger; with $n_8 = 0.12$ and $x_e = 0.1$, the flux would be $F_\lambda \approx 4.8 \times 10^{-17}$ ergs s^{-1} cm^{-2} $Å^{-1}$, much smaller than the observed

value $\sim 3.6 \times 10^{-15}$ ergs s^{-1} cm^{-2} Å^{-1}. As long as the ionization arises from nonthermal energy deposition and photoionization by UV photons from the interior of the nebula, the electron fraction is unlikely to be large enough to produce the observed Hα flux. Because of the observed time evolution of the Hα flux, it seems clear that ionization by circumstellar X-rays is relatively unimportant until age 300 days.

Our synthetic spectrum calculations indicate that, at 140 days, the observed flux at Hα ($F_\lambda \approx 10^{-14}$ ergs s^{-1} cm^{-2} Å^{-1}) is a blend of Hα and several weaker lines of Fe I and Fe II, with Hα providing about 30% of the flux. This is produced in 0.3 $M_\odot$ of envelope material with hydrogen and helium mass fractions $X = 0.42$ and $Y = 0.57$, respectively, and density $n = 5.7 \times 10^7$ cm^{-3}, temperature $T = 8500$ K, and electron fraction $x_e = 0.1$. The level populations in H I are $x_2 = 3.5 \times 10^{-8}$ and $x_3 = 1.6 \times 10^{-12}$. These values are well reproduced by numerical solution of equations (8a)–(8d) when an Hα pumping intensity $J_{32} = 4 \times 10^{-8}$ ergs s^{-1} cm^{-2} Hz^{-1} sr^{-1} is included. This is somewhat larger than the value estimated from the observed spectrum, but still in line with expectations. Figure 3 shows the time evolution of the observed value of the flux at Hα compared with various semianalytic estimates of the Hα flux. The curves are labeled according to which Hα production mechanisms contribute to the emission. Each of the analytic models includes a constant emission component, attributed to the circumstellar interaction contribution, equal to the mean observed Hα flux after age 350 days (Fransson & Houck 1995). From this figure, it is clear that recombination alone is insufficient to produce the observed Hα emission at 140 days and that the rate of decrease of the Hα luminosity is much too rapid in this case. In contrast, the observed slow decline in Hα is much better reproduced by models which include line scattering. We emphasize that our detailed spectrum calculation indicates that the observed feature at Hα contains an important contribution from blended iron lines, so that the observed flux at Hα is significantly larger than the actual Hα intensity. The figure shows that this simplified model agrees closely with the more detailed calculation, and that scattering of oxygen photons at a level consistent with the observed line intensity explains the observed behavior of Hα.

6.1.5. Hα *Absorption in High-Velocity Hydrogen*

When Hα is optically thick, scattering of the redshifted [O I] λλ6300, 6364 photons produces a strong absorption feature in the [O I] λλ6300, 6364 line profile. Because the width of this absorption feature corresponds to the velocity thickness of the optically thick part of the hydrogen envelope, this feature provides a way of directly measuring the thickness of the hydrogen envelope. The location of the blue edge of the Hα scattering feature determines the highest velocity at which Hα is optically thick, while the location of the red edge determines the velocity at the corresponding position at the base of the hydrogen envelope. The width of this absorption feature and its behavior over time constrain the mass of the H/He envelope and its extent in velocity.

By inspection, the observed Hα absorption lies (roughly) between 6340–6390 Å, indicating that the bulk of the hydrogen envelope lies somewhere between 7900–10,000 km s^{-1}. The line center of the [O I] λ6364 component of the doublet is heavily absorbed, while only the red wing of the [O I] λ6300 component is absorbed. Scattering features associated with Hβ and Hγ are also present in the observed spectra. Blueshifted absorption by Hβ is prominent between 4696–4742 Å prior to 140 days (1993 August 15), although it is no longer present at 177 days (1993 September 20). The position and width of the Hβ absorption feature correspond to a velocity range of $\sim$7400–10,000 km s^{-1}, consistent with the observed Hα absorption. Although the Hβ feature is relatively close to the Mg I] λ4571 line, it does not come into resonance with that line because the required Doppler shift is too large ($\sim$18,000 km s^{-1}). In particular, Hβ absorption is not responsible for the apparent similarity between the Mg I] and [O I] λλ6300, 6364 profiles interpreted by Spyromilio (1994) as evidence for large-scale asymmetries. Prior to age 100 days, blueshifted Hγ absorption is clearly present between $\sim$4200–4233 Å, corresponding to a velocity width $\sim$7400–9700 km s^{-1}. However, because this feature is weaker and because it coincides with another dip in the spectrum, perhaps an absorption by the Fe II resonance a line at 4234 Å corresponding to Fe II $^4_bP_{5/2}$–$^4_zD_{7/2}$, its precise extent and its behavior over time are less clear than for Hβ and Hα. We note that the features that we identify as absorption by Hα, Hβ, and Hγ are not all centered at exactly the same velocity relative to the rest wavelength, nor are the profiles identical. For example, the Hα absorption is centered at about 8900 km s^{-1}, the Hβ feature is centered at about 8500 km s^{-1}, and the Hγ feature is centered at about 9000 km s^{-1}, although the latter is uncertain. The widths and profiles differ at about the same level and show similar changes over time. We attribute this variation to differences in the background of emission and changes in this background as a function of time. Because the Hα feature is the most prominent, and because it is in resonance with a strong feature in a relatively uncomplicated blend, it is the easiest of these features to analyze. In the following, we use the Hα absorption feature to constrain the mass and thickness of the H/He envelope.

While the population of $n = 3$, and therefore the Hα luminosity, is strongly dependent on line blending effects, the population of $n = 2$ and thus the Hα optical depth are determined mainly by the balance between recombination and photon emission, with some contribution from direct nonthermal excitation. From equations (8a)–(8d), the population of $n = 2$ is then

$$x_2 \approx (1 - x_e)\left(\frac{\Gamma_{12} + \Gamma_I}{A_{2\gamma} + A_{21}\beta_{21}}\right). \tag{10}$$

The Sobolev optical depth of Hα is

$$\tau_{\mathrm{H}\alpha} = \frac{A_{32}\lambda_{32}^3 t}{8\pi g_2} g_3 n_2 \equiv h_{32} t n x_2 , \tag{11}$$

while for Lyα, the optical depth may be written $\tau_{21} \equiv h_{21} t n x_1 \approx h_{21} t n (1 - x_e)$, because $x_2 \ll 1$.

Combining equations (10) and (11) and noting that $\beta_{21} \approx 1/\tau_{21}$ because $\tau_{21} \gg 1$, we obtain

$$n = \frac{n_a}{2}\left[1 + \left(1 + \frac{4n_b}{n_a}\right)^{1/2}\right], \tag{12}$$

where

$$n_a \equiv \frac{A_{2\gamma}\tau_{\mathrm{H}\alpha}}{(\Gamma_{12} + \Gamma_I)h_{32}(1 - x_e)t},$$

$$n_b \equiv \frac{A_{21}}{A_{2\gamma}h_{21}(1 - x_e)t}.$$

To the extent that the hydrogen number density is $\ll 2 \times 10^8$ cm^{-3}, two-photon emission is slow compared to Lyα emission, $4n_b/n_a \gg 1$ and $n \approx (n_b n_a)^{1/2}$. We estimate that the hydrogen envelope density is (3–5) $\times 10^7$ cm^{-3} at 140 days, so that Lyα emission is ~ 5 times faster than two-photon emission. This is in contrast to the case of SN 1987A. The Hα optical depth can then be written

$$\tau_{\mathrm{H}\alpha} \approx 4.9 n_7^2 (1 - x_e)^2 e^{-\tau_{\gamma,c} v_4^{-2}} \left(\frac{\chi_{\mathrm{eff}}}{60\ \mathrm{eV}}\right)^{-1} \times \left[\frac{M(^{56}\mathrm{Ni})}{0.08\ M_\odot}\right] e^{-t/111\ \mathrm{days}}, \quad (13)$$

where n_7 is the hydrogen number density in units of 10^7 cm^{-3}.

Equation (13) relates the Hα optical depth to the hydrogen density in the H/He envelope. At 140 days, our detailed model has $\tau_{\gamma,c} = 0.5$ for $v_4 = 0.9$. Our calculations also indicate that the electron fraction is $x_e \approx 0.1$ between 140 days and 300 days. Taking the hydrogen density in the H/He envelope $n_7 = 4.5$ at 140 days, the Hα optical depth is $\tau_{\mathrm{H}\alpha} = 17$. Consistent with the above discussion, this implies that scattering in the Balmer lines should be efficient. At 250 days, assuming that $\tau_{\gamma,c} \propto t^{-2}$ and $n_7 \propto t^{-3}$, the Hα optical depth is $\tau_{\mathrm{H}\alpha} \lesssim 0.02$. Therefore, while the scattering absorption feature is strong at 140 days and at earlier times, it should disappear by age 250 days because of the decrease in density and nonthermal energy deposition. This agrees closely with the observed behavior and with the results of our synthetic spectrum calculations.

In terms of the Hα optical depth, the Balmer continuum depth is

$$\tau_{\mathrm{B}} \approx 0.013 \tau_{\mathrm{H}\alpha} v_4 \left(1 - \frac{V_{\mathrm{min}}}{V_{\mathrm{max}}}\right), \quad (14)$$

where V_{min} and V_{max} represent the velocity range of the part of the hydrogen envelope sampled by the Hα absorption feature. For hydrogen at high velocities, $\tau_{\mathrm{B}} \approx 0.02 \ll 1$ at 140 days. Although $\tau_{\mathrm{B}} \ll 1$, the photoionizing flux in the Balmer continuum is significant. Therefore, Balmer continuum photoionization remains important, producing about half of all hydrogen ionizations.

While the presence of Hα absorption in some wavelength range within the [O I] $\lambda\lambda$6300, 6364 blend is a clear indication that Hα is optically thick in the corresponding velocity range, the *absence* of a scattering feature in some nearby wavelength range (within this O I blend) indicates that $\tau_{\mathrm{H}\alpha} \lesssim 1$ at the corresponding velocity. From equation (13), the hydrogen density at that corresponding velocity must be smaller than

$$n_{\mathrm{max}} \approx 1.43 \times 10^6 (1 - x_e)^{-1} e^{\tau_{\gamma,c}/2} v_4 \left(\frac{\chi_{\mathrm{eff}}}{60\ \mathrm{eV}}\right)^{1/2} \times \left[\frac{M(^{56}\mathrm{Ni})}{0.08\ M_\odot}\right]^{-1/2} e^{t/222\ \mathrm{days}}\ \mathrm{cm}^{-3}. \quad (15)$$

In contrast to the number density in the nebula, which decreases as $n \propto t^{-3}$, this upper limit on the number density is relatively insensitive to the age between $\sim$50–300 days. Therefore, at early times $\sim$50 days, this upper limit on the hydrogen density allows us to constrain the mass of hydrogen at intermediate velocities, in the range for which Hα is in resonance with [O I] $\lambda\lambda$6300, 6364.

Equation (15) constrains the hydrogen mass outside 8500–10,000 km s^{-1}. Observations of SN 1993J indicate that the oxygen shell extends out to $\sim$4000 km s^{-1} so that the blue wing of the [O I] $\lambda\lambda$6300, 6364 blend extends to $\sim$6220 Å, while the red wing extends to $\sim$6450 Å. The Hα absorption feature is present between 6340–6390 Å as early as 50 days after the explosion and maintains the same width until Hα becomes optically thin and the feature fades away at age 220 days. Because no strong absorption is present between 6220 Å and 6340 Å during this time period, one concludes that the hydrogen density between (1.02–1.57) $\times 10^4$ km s^{-1} is small enough so that $\tau_{\mathrm{H}\alpha} < 1$ in this wavelength range, even as early as 50 days after the explosion. At an age of 50 days, with $v_4 = 1.1$, $\tau_{\gamma,c} = 3.9$, and $x_e = 0.15$, Hα is optically thin only if the hydrogen density is less than $n_{\mathrm{max}} = 1.4 \times 10^8$cm^{-3}. A uniform shell at this density between (1.0–1.5) $\times 10^4$ km s^{-1} would contain only 0.06 $M_\odot$ of hydrogen. Similarly, because no strong absorption is present between 6390 Å and 6450 Å between 50–220 days, the hydrogen density in the corresponding velocity range 5600–7900 km s^{-1} must be small enough to ensure that $\tau_{\mathrm{H}\alpha} < 1$, as early as 50 days after the explosion. At an age of 50 days, with $v_4 = 0.6$, $\tau_{\gamma,c} = 2$, and $x_e = 0.15$, Hα is optically thin only if the hydrogen density is less than $n_{\mathrm{max}} = 4.7 \times 10^7$ cm^{-3}. A uniform shell of this density between 5600–7900 km s^{-1} would contain $<0.01\ M_\odot$ of hydrogen. We conclude that, because no clearly observable absorption feature is present in the [O I] $\lambda\lambda$6300, 6364 blend, only a negligible mass of neutral hydrogen is present between 5600–7900 km s^{-1} or (1.02–1.57) $\times 10^4$ km s^{-1}. Here we have derived these constraints from the constant width of the absorption after age 50 days; in general, the earlier the stage at which one can use this argument to constrain the number density in the hydrogen envelope, the stronger the constraint one can set. We emphasize that we have not produced detailed spectrum models valid at age 50 days. We merely point out that the Hα absorption feature can be traced from this early epoch and argue on the basis of continuity; i.e., that the absorption is produced by the same physical transition, namely, Hα, at both early and late times.

Deriving the velocity thickness of the H/He envelope directly by inspection of the observed spectra is a bit uncertain because the precise extent of the absorption feature is unclear. Synthetic spectrum models with the observed feature indicate that the hydrogen envelope should lie between $\sim$8000–10,000 km s^{-1}. This velocity range is rather well determined; we rule out the presence of more than 0.02 $M_\odot$ of hydrogen above or below this range because that amount of material would produce a noticeably broader absorption feature, in disagreement with the observed spectrum.

As expansion decreases the Hα scattering efficiency, the scattering absorption feature becomes less prominent. Because the density in the hydrogen envelope should decrease outward, one expects the absorption feature to narrow from the blue edge with time as Hα becomes optically thin at lower and lower velocities. The decrease in depth of the absorption feature is apparent in the observed spectra covering the period from August 15 (140 days) to November 7 (224 days). On August 15 (140 days), the Hα absorption is quite deep; on September 20 (177 days), the depth is significantly reduced, and by November 7 (224 days) the absorption has disappeared. The feature also appears to narrow slightly from the blue edge as expected, although the effect is small. Because the observed absorption feature disappeared at an age of $\sim$225 days, the hydrogen density of the envelope material in which this absorption formed must be $n_{\mathrm{max}}(225\ \mathrm{days}) \approx 2 \times 10^7$ cm^{-3} at

this epoch. This implies a total hydrogen mass between 8500–10,000 km s^{-1} of only $\lesssim 0.2\ M_\odot$ or a H/He envelope mass of $\lesssim 0.5\ M_\odot$, assuming significant helium enrichment so that the hydrogen and helium mass fractions are $X = 0.42$ and $Y = 0.57$, respectively. This is necessarily an overestimate of the envelope mass, probably by at least a factor of 2, because we have used $\tau_{H\alpha} = 1$ as the optical depth when the absorption feature disappears; if $\tau_{H\alpha} = 1$, an absorption feature would still be observed because the oxygen emission would be reduced by a factor of e. Extrapolating back to age 50 days, the hydrogen density would have been $n_H \lesssim 1.8 \times 10^9$ cm^{-3}, more than an order of magnitude larger than the limit set above on the hydrogen density outside 8500–10,000 km s^{-1}. Therefore, the shape of the observed absorption feature constrains the hydrogen envelope to have relatively sharp edges where the hydrogen density falls by more than an order of magnitude.

6.2. *Helium*

The most prominent helium feature in the late optical spectra is He I λ5876. In our models at 140 days, this feature is typically a blend of He I λ5876 ($\sim$50%) and Na I $\lambda\lambda$5890, 5896 ($\sim$30%), with the remainder coming mainly from Fe II lines. He I λ6678 is obscured by Hα emission and, while He I λ7065 is present, only its blue edge is visible in a blend with [Ca II] λ7307. Other helium lines at 5017 Å and 4472 Å are so thoroughly blended with iron lines that we are unable to extract quantitative information on the line shapes and intensities. Our calculations indicate that, at 140 days, He I $\lambda = 1.083$ μm should be reasonably bright (Fig. 10), with $F_\lambda \approx 0.51 \times 10^{-14}$ ergs s^{-1} cm^{-2} $Å^{-1}$ and width comparable to He I λ5876. The red wing of He I $\lambda = 1.083$ μm blends with the much weaker [Si I] $\lambda = 1.1$ μm line [F_λ([Si I])/F_λ(He I) ≈ 0.1], and a still weaker [Co II] $\lambda = 1.098$ μm line, but otherwise this feature appears unblended. The He I line fades relative to the [Si I] line, so that at 284 days, He I $\lambda = 1.083$ μm has $F_\lambda \approx 0.039 \times 10^{-14}$ ergs s^{-1} cm^{-2} $Å^{-1}$, and F_λ([Si I])/F_λ(He I) ≈ 0.25.

Optical depth effects in He I λ3888 and He I λ3187 are important in determining the helium triplet line ratios, so that He I λ7065 and He I λ4713 are significantly enhanced relative to the intensities found in case B recombination. Optical depth effects are also important in singlet line formation, for He I λ5017 and He I λ6678. Although the helium lines are produced mainly as a result of recombination, these optical depth effects imply that a pure recombination approximation is not justified for the individual lines, and a more sophisticated calculation similar to that in this paper is necessary.

While the helium mantle in the explosion model extends out to $\sim$8600 km s^{-1}, the bulk of the helium emission in the observed spectra and in our calculations arises below 5000 km s^{-1}. Because the emission from helium at higher velocities is relatively weak, the calculated line profiles have broad, weak tails which blend with nearby emission. The brighter component of the profile has a half-width roughly consistent with the observed line profile. Therefore, the observed line widths do not give a clear indication of the maximum expansion velocity of the helium mantle. As a result, neither the optical nor the infrared spectrum between 100–400 days places interesting direct limits on the total helium mass.

While the optical spectrum provides few clues to the helium mass, it can be constrained because the oxygen mass is a sensitive function of the helium core mass (e.g., Nomoto et al. 1993). Given that the 4.0 $M_\odot$ helium core model 4H 47 produced

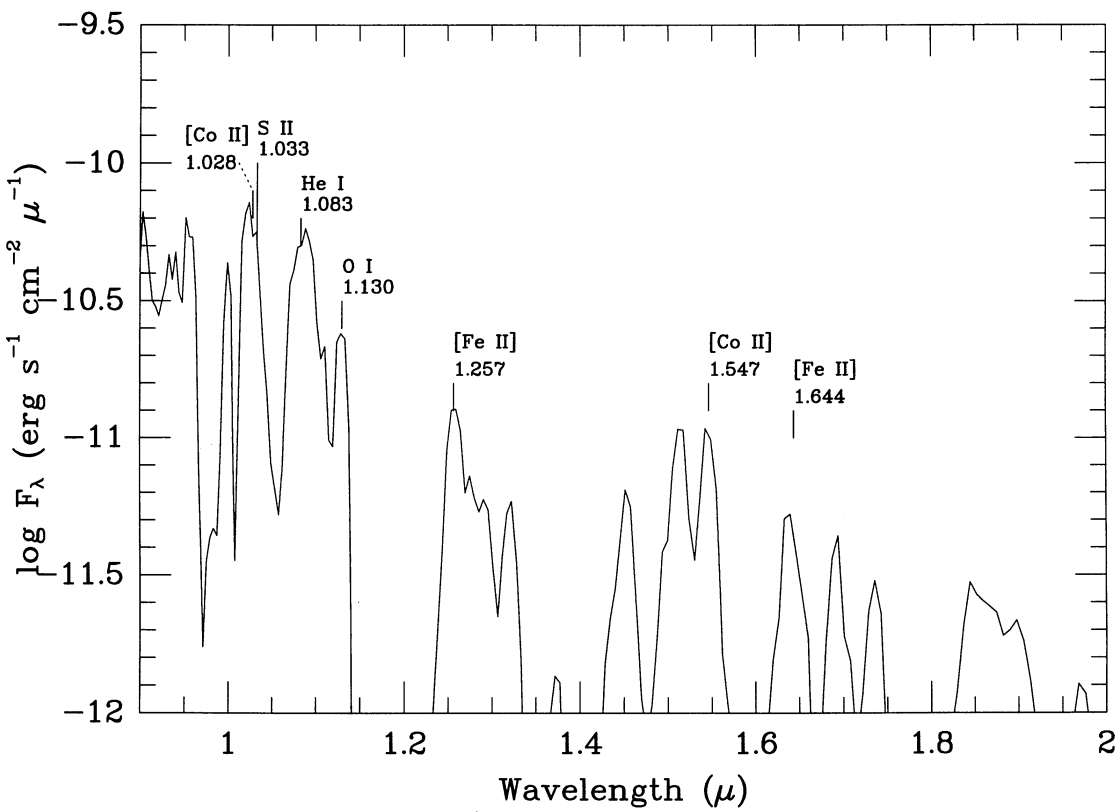

FIG. 10.—Synthetic IR spectrum at age 140 days (1993 August 15) with line identifications

about the right oxygen mass, this model probably gives a good representation of the helium mass as well. In addition to its effect on the oxygen mass, significantly increasing the helium mass in model 4H 47 would require significantly more than 10^{51} ergs in kinetic energy if the overall expansion velocity is maintained consistent with the observed line widths. A constant velocity helium shell of $M_{\rm He}$ solar masses has kinetic energy $E_K = 4 \times 10^{51} M_{\rm He} v_4^2$ ergs, so that an additional solar mass of helium at a velocity of 5000 km s^{-1} would require an additional 10^{51} ergs of energy. Furthermore, a large mass of helium at low velocity would significantly dilute the gamma-ray flux in the Fe/O core, in conflict with the observed spectrum. In this case, the He I lines would have been stronger and narrower than was observed.

6.3. *Oxygen*

In principle, the [O I] $\lambda\lambda$6300, 6364 doublet line ratio can be used to infer the density in the oxygen emitting region (e.g., Spyromilio & Pinto 1991). Unfortunately, the high degree of blending of the doublet components and the strong absorption of [O I] λ6364 by Hα in the H/He envelope makes this diagnostic very uncertain. Using the December 17 spectrum, we estimate that the line ratio is $I(6300)/I(6364) \approx 2$, although this is only an uncertain lower limit. Given the uncertainty involved, we conclude that the blending is too severe to allow a meaningful result. Our models fit the observed spectrum without extensive clumping and with only $\sim 0.5\ M_\odot$ of oxygen. The oxygen-rich material in these models typically has $n \approx 10^8$ cm^{-3}. In contrast, models with extensive clumping in which the oxygen rich material had a density of $n \approx 5 \times 10^9$ cm^{-3} produced strong [O I] λ5577 and O I] λ6726 emission, completely unlike the observed spectrum. At this epoch, therefore, we infer that the density in the oxygen-rich material is $\ll 5 \times 10^9$ cm^{-3}, so that [O I] $\lambda\lambda$6300, 6364 is nearly optically thin.

Compared with the observed spectra, our models consistently underestimate the O I line ratio $I(9264)/I(7771)$. At 140 days, the O I λ7771 transition is optically thick, with Sobolev optical depth $\tau_{7771} \gtrsim 10$. O I λ9264 remains optically thin, with $\tau_{9264} \approx 0.1$. Using collision strengths from Carlsson (1993), computed using the impact parameter approximation of Seaton (1962), we find that collisional excitation of O I λ7771 is slow compared to recombination. Because collisional deexcitation is inefficient and no alternate downward path is available, the line ratio should be determined by the excited state recombination rates. Because our computed line ratio is inconsistent with the observed ratio, we suggest that the relevant quintet recombination rates taken from Escalante & Victor (1992) are inaccurate. Based on the observed value of the O I line ratio $I(9264)/I(7771) \approx 0.8$, the bulk of the O I quintet recombinations seem to enter the $3d\,^5D$ state, producing the 7771 Å feature in the downward cascade.

6.4. *Magnesium*

In the optical, the only clear feature attributable to magnesium is Mg I] λ4571. In our spectrum model at 140 days, the strength of this feature is reasonably well represented, although the detailed line profile is poorly reproduced. The computed line profile is rather jagged because of overlapping, narrow Fe absorption lines. While absorption features can be seen in the observed Mg I] λ4571 profile, they are much smaller, indicating that we have overestimated the optical depth of the relevant absorbing line transitions, particularly Fe II $^4_zD \rightarrow {}^4_bF$ $\lambda\lambda$4509–4621.

Aside from the effects of overlapping iron absorption and emission features in this region of the spectrum, the difficulty in reproducing the observed Mg I] λ4571 feature is compounded by uncertainties in the magnesium ionization balance.

First, there are large variations in available recombination rates. The older rates of Aldrovandi & Péquignot (1973) are a factor of 3 larger than the more recent rates from Shull & Van Steenberg (1982). Our calculations, using the newer rates, reproduce the observed Mg I] λ4571 flux at age 140 days reasonably well but underproduce it by more than a factor of 3 at 284 days. If we use the older rates, the line flux at 140 days is overproduced by an order of magnitude, although the flux at 284 days is better fit. Because we are unable to fit the line strength at both epochs with a single set of recombination rates, it appears that we do not accurately model the time evolution of the ionization balance. This is most likely coupled with the sensitivity of the Mg I abundance to the radiation field.

With its low ionization threshold, Mg I is quite sensitive to the photoionizing radiation field. Because the $3p\,^3P$ excited state is metastable, its population is relatively large, and photoionization from this excited state by photons above ~ 5 eV is important. The line strength is therefore sensitive to the detailed UV radiation field below 2518 Å, in particular, the C II] λ2326 line. Photoionization from the ground state is complicated by the unusual energy dependence of the ground state photoionization cross section near 9.4 eV (Butler, Mendoza, & Zeippen 1993). The most plentiful source of photons for ionizing Mg I from the ground state is O I] λ1355, corresponding to a photon energy of 9.2 eV. Because the ground state photoionization cross section has a deep minimum near this energy, ionization of Mg I by O I] λ1355 photons is inefficient. Instead, the O I] photons strongly ionize Si I, which has a photoionization cross section more than ~ 500 times larger than that of Mg I at this energy. If the position of the minimum in the (theoretical) cross section were in error by as much as 0.5 eV, the photoionization cross section at 1355 Å, and the corresponding Mg I photoionization rate, could increase by a factor $\gtrsim 10$, reducing the Mg I abundance by a similar factor. Because Butler et al. claim that their calculated cross section is in good agreement with experiments, such a large discrepancy may be unlikely.

Finally, the magnesium abundance may be a factor of ~ 2 lower than in the model, perhaps as a result of the uncertain $^{12}C(\alpha, \gamma)^{16}O$ rate. While important for producing the observed spectrum, the uncertainty in the Mg I abundance has little effect on the energy balance or electron fraction in the oxygen-rich material, since cooling is dominated by Mg II and O I and since the magnesium abundance is $\lesssim 8\%$ by number.

6.5. *Iron and Cobalt*

Emission between 4000–5500 Å is dominated by emission from [Fe I] and [Fe II]. At a temperature ~ 4500 K, the optical lines (4000–5000 Å) associated with the ground term of Fe II are mainly collisionally excited, while the corresponding ground term UV lines (2000–2500 Å), which indirectly feed other optical lines between 4000–5500 Å, are excited both by thermal electron collisions and recombination. Absorption of UV line photons from other parts of the ejecta and subsequent reemission of optical photons is also important (§ 5.2). Much of the remaining optical emission between 4000–5500 Å arises

from the recombination cascade of Fe II after nonthermal ionization, and from collisional excitation of optical lines of Fe III. While the strength of individual features is somewhat uncertain because of the relatively uncertain atomic data (the recombination rates in particular), the integrated iron emission in this wavelength region provides an indication of the nonthermal energy deposition in the iron core material.

The presence of narrow emission lines of iron and cobalt, which provided a diagnostic in support of mixing, depends somewhat sensitively on the velocity at the mass cut associated with neutron star formation. Current explosion models do not self-consistently determine this velocity. Nevertheless, the presence of narrow peaks on the Ca II emission lines indicates that Ca-Fe–rich material must be present at low velocities (~ 1000 km s^{-1}). Because calcium is produced just outside the iron core in the explosion models, consistency with explosion models would imply that, in the absence of mixing, the bulk of the iron core material must occupy lower velocities. We have shown that such a low-velocity iron core leads to the production of bright, narrow Fe I and Co I emission lines, inconsistent with the observed spectra. Thus, while the narrow calcium emission line peaks indicate that some calcium-emitting material must lie at low velocities $\lesssim 1000$ km s^{-1} (the observed line widths also indicate that Ca II emission extends out to ~ 4000 km s^{-1}), consistency with the observed spectrum leads to the conclusion that the iron core material must be mixed outward to velocities $\gtrsim 3000$ km s^{-1}.

Most of the optical emission from the iron core material comes from Fe II and Fe III. Although the Fe I abundance is relatively low [n(Fe I)/n(Fe) ≈ 0.001–0.02], many of its optical resonance transitions have large optical depths $\tau \gtrsim 10$ even at 284 days; a number of metastable Fe II optical transitions have $\tau \sim 1$–10 as well. A typical example of line blending is Fe II $^4_zD \rightarrow {}^4_bF$ $\lambda\lambda 4509$–4621, which absorbs Mg I] $\lambda 4571$. The Fe II $^4_zD_{7/2} \rightarrow {}^4_bF_{9/2}$ $\lambda 4585$ transition has Sobolev optical depth $\tau \approx 17$ at 140 days, decreasing to $\tau \approx 0.5$ at 284 days. Because many transitions between 4000–5500 Å remain optically thick even at late times ~ 250 days, line blending effects must be included in detailed models. However, given the relative inaccuracy of the available atomic data on iron ions, line blending further increases the uncertainty involved in calculating the strength of individual features in this complex.

During the first year after the explosion, the far-infrared, fine-structure lines of iron and cobalt are relatively weak, primarily because of the high temperature. In units of 10^{-18} ergs s^{-1} cm^{-2} Å^{-1}, typical [Fe II] line strengths at 140 days are 1.8 (17.9 μm) and 0.7 (26 μm). The near-infrared lines are much brighter (Fig. 10), having intensities of 410 (1.26 μm), 230 (1.66 μm), and 16.2 (2.1 μm). While the temperature is above ~ 3000 K, collisional cooling caused by iron peak elements is dominated by optical emission. When the temperature in the iron core material falls below ~ 3000 K, fine-structure cooling gradually dominates, leading to an "infrared catastrophe" in which the iron core material rapidly cools down to ~ 250 K within ~ 200 days (Axelrod 1980; Fransson & Chevalier 1989; Fransson, Houck, & Kozma 1994). At 327 days, the temperature in the iron core material is ~ 3500 K, so that fine-structure cooling is becoming stronger. The far-infrared [Fe II] lines are significantly stronger compared to age 140 days, with line strengths 7.2 (17.9 μm) and 2.1 (26 μm), while the near-infrared lines are weaker, having line strengths 244 (1.26 μm), 137 (1.64 μm), and 2.8 (2.1 μm). While optical emission still dominates at an age of about a year, fine-structure cooling is becoming more important and is likely to dominate by age 550–600 days.

The recombination cascade of neutral and singly ionized iron and cobalt in the iron core provides an important source of ionizing photons in the supernova. Photons with energies in the Balmer continuum (> 3.4 eV) but below the Fe I ionization potential (7.87 eV) are particularly important for photoionization of hydrogen in the H/He envelope as well as excited state photoionization of Mg I. If the Fe I continuum is optically thin, the more energetic photons with energies above ~ 8 eV escape the iron core and contribute to the photoionization of species with low ionization potentials, Mg I in particular (§ 6.4). At age 140 days, the Fe I ground state continuum optical depth near threshold is $\tau_{\rm Fe} \gtrsim 10$, while the continua from excited states are thin. At lower densities, the Fe I fraction decreases enough to make the ground-state continuum optically thin.

We briefly mention two problematic aspects of multilevel solutions for iron and cobalt ions. First, accurate rates for recombination to excited states of Fe II and Co II do not exist; excited state recombination rates must be estimated (see Appendix). Therefore, special care must be taken in modeling the recombination cascade in spectrum calculations which model neutral or singly ionized iron and cobalt with relatively few, low-lying excited states. In particular, if all recombinations go to the ground state, producing photons well above the Balmer continuum threshold, these energetic continuum photons ionize hydrogen only inefficiently, resulting in a significant underestimate of the Balmer continuum ionizing flux. At present, even if large model atoms are used, the recombination cascade is poorly determined because of the lack of excited state recombination rates. Collisional contributions to these high states are, however, unimportant. We feel that this is the main uncertainty of our calculation.

Second, our synthetic spectra tend to overproduce cobalt emission features, probably because of inaccuracies in the atomic data, especially the collision strengths, for cobalt ions. For example, at 140 days, Co II provides more than 60% of the collisional cooling in the iron core material, while iron emission contributes only $\sim 10\%$. In the optical spectra, the most obvious result of this is the relatively bright [Co II] emission line at 9569 Å which is clearly not present in the observed spectra. The largest uncertainties in the atomic data for cobalt ions lie in the collision strengths, so that the worst errors occur in collisionally excited lines in the optical and infrared. Because of coupling between atomic levels, the computed emissivities of transitions with better determined collision strengths may also be affected. We tested the influence of cobalt on the synthetic spectrum by computing a model spectrum at age 140 days in which cobalt emission was neglected. The deficit in cooling was made up by Fe II emission, causing the temperature in the iron core material to increase slightly to ~ 4900 K. The largest change in the optical spectrum was a factor ~ 2 brightening in the Fe II emission at 5300 Å. Other iron features brightened to a lesser degree. The rest of the optical spectrum was relatively unchanged. Therefore, while the computed strength of especially the 5300 Å feature is uncertain, the temperature determination in the iron core material is relatively insensitive to this uncertainty. Nevertheless, this may be a significant problem for temperature-sensitive line ratios such as Ca II $I(7307)/I(8582)$.

We also tested the sensitivity of our results to the number of levels included in our Fe II model atom. At 140 days and 284 days, we compared models with two different Fe II model atoms, one with 121 energy levels and one with 191 energy

levels. In the larger atom, a number of the transition probabilities were updated using newer values from Nahar (1995). At each epoch, the spectra computed with the larger model atom were little different from the spectra computed using the smaller model atom. Furthermore, the physical conditions in the iron-rich material were essentially the same. Baron & Hauschildt (1995) have discussed the importance of including the many weak transitions in iron peak ions. That our results are insensitive to the addition of 70 further energy levels to the Fe II atom indicates that spectrum formation under these conditions is not strongly affected by interactions involving highly excited states of Fe II. This is mainly attributable to the relatively low temperatures involved, $\lesssim 10^4$ K, and to the low opacity of these additional transitions.

6.6. *Other Elements*

The most prominent spectral feature associated with carbon is [C I] λ8727, heavily blended with the Ca II triplet. Most of the [C I] emission arises from the C/O zone at velocities $\lesssim 3900$ km s^{-1}, although about 20% is produced in the denser parts of the helium envelope, out to ~ 5300 km s^{-1}. Our synthetic spectrum indicates that the redward edge of the [Ca II]–[C I] blend is dominated by [C I] emission, allowing an estimate of the expansion velocity of the C/O material. Consistent with the shape of the observed blend at 140 days, our synthetic spectrum places the red edge of this blend at 8836 Å. This calculation also indicates that the red edge of the [Ca II] emission lies well inside the observed blend, close to 8780 Å. Therefore, the estimate of the velocity range of [C I] emission is not confused by redshifted emission from the 8662 Å component of the Ca II triplet. We conclude that most of the carbon is confined to velocities $\lesssim 3900$ km s^{-1} and that the total mass of carbon is probably close to that produced in model 4H 47, about 0.1 $M_\odot$.

As discussed by Fransson & Chevalier (1989), the character of the emission from the oxygen-rich material is sensitive to the relative abundances of oxygen and calcium. If the calcium to oxygen abundance ratio is as high as 10^{-3}, calcium dominates the cooling. Because the relative abundance of calcium is sensitive to the degree and character of convective mixing in the progenitor star, the exact abundance is uncertain, as is apparent from models of SN 1987A (Hashimoto, Nomoto, & Shigeyama 1989; Woosley 1988). Increasing the calcium abundance in the oxygen-rich material to $n(\mathrm{Ca})/n(\mathrm{O}) = 10^{-3}$ lowered the temperature to $T = 4500$–5000 K. This led to relatively broad profiles for the Ca II features at 7300 and 8550 Å which clearly did not fit the narrower, more sharply peaked profiles in the observed spectrum. Furthermore, the Ca II line ratio $I(7300)/I(8550) > 1$, while the observed line ratio $I(7300)/I(8550)$ was less than unity. From comparison with the observed spectrum, therefore, we conclude that the calcium to oxygen abundance ratio in the oxygen-rich material of SN 1993J is smaller than 10^{-3}.

7. LINE PROFILE ASYMMETRIES

The observational evidence for asymmetries in the ejecta of SN 1993J has rested on the overall structure of prominent spectral features such as the [O I] $\lambda\lambda$6300, 6364 blend and on the smaller scale structure of these individual features. Based on his examination of similarities in the shape and position of features identified as [O I] $\lambda\lambda$6300, 6364, [O I] λ5577, and Mg I] λ4571, Spyromilio (1994) concluded that *large-scale asymmetries* must be present. A similar conclusion was reached by Lewis et al. (1994) and by Wang et al. (1993). In § 6.1.5 we showed that Hα scattering is responsible for the apparently asymmetric position of the [O I] $\lambda\lambda$6300, 6364 blend. Therefore, this feature can be explained in terms of a spherically symmetric model in which oxygen and hydrogen are confined to reasonably well defined shells, in contrast to a model in which the oxygen distribution is highly asymmetric. Similarly, the [O I] λ5577 and Mg I] λ4571 profiles discussed as evidence for asymmetries by Spyromilio (1994) can also be understood as the result of line blending and overlapping absorption features.

The feature identified as [O I] λ5577 is likely to be a blend of [O I] λ5577, [Fe II] λ5536, and [Co II] λ5526. Because the Fe and Co lines are comparable in strength to the [O I] λ5577 line and overlap its blue wing, a blend of these flat-topped lines produces a relatively sharp peak just blueward of [O I] λ5577, consistent with the blueshifted, narrow ~ 150 km s^{-1} wide peak observed at 140 days (Fig. 2). While the oxygen features can all be understood in terms of a fairly ordered distribution of oxygen in a spherical shell between 1000–4000 km s^{-1}, the O I λ7771 and O I λ9264 lines do appear to be slightly blueshifted, although the velocities inferred are less than 500 km s^{-1}, much smaller than the 1500 km s^{-1} asymmetries discussed by Spyromilio. Because line blending does not seem to be important here, this apparent blueshift may be indicative of real asymmetries, possibly related to large-scale mixing.

As discussed in § 6.5, the Mg I] λ4571 feature is strongly affected by optically thick Fe II $^4_zD \rightarrow {}^4_bF$ and $^4_zF \rightarrow {}^4_bF$ multiplets near 4600 Å. This scattering of the Mg I] λ4571 photons, especially in the red wing of the Mg I] λ4571 line, produces an absorption feature similar to that produced by Hα in the [O I] $\lambda\lambda$6300, 6364 blend. While our models do not fit this profile particularly well, it seems apparent that the profile behavior can be explained relatively simply in terms of line blending, entirely analogous to the [O I] $\lambda\lambda$6300, 6364 case.

In contrast, the explanation of the Mg I] profile in terms of large-scale asymmetries (Spyromilio 1994) poses serious problems. Standard explosion models imply that magnesium and oxygen are co-spatial. Interpreting the small bump redward of Mg I] λ4571 as emission from a blob of Mg I with a highly asymmetric velocity, the velocity inferred from the blue edge of this bump is ~ 1400 km s^{-1}. Interpreting the small bump redward of the 6300 Å feature (which we believe is attributable to Hα and [O I] λ6364 emission) in the same way, one infers a velocity of ~ 2400 km s^{-1}. The inconsistency in the inferred velocities between the Mg I] and the [O I] profiles does not rule out a large asymmetry, but it does make it less likely that these two features come from the same asymmetry in the way Spyromilio suggests.

While the apparent large-scale asymmetries in the more prominent observed spectral blends can be understood as a result of line blending, the origin of the smaller scale features associated with individual blends is less clear. Perhaps the best example of this persistent small scale structure is associated with the [O I] $\lambda\lambda$6300, 6364 blend (see also Matheson, Filippenko, & Ho 1995). The most prominent of these smaller features are the ~ 1000 km s^{-1} wide dips at 6280 Å and 6297 Å which persist in the [O I] $\lambda\lambda$6300, 6364 profile from at least ~ 100 days to ~ 416 days. The most prominent dip, near 6280 Å, is clearly present at age 72 days and may be present much earlier, although rapid changes in the background of emission at early times make identification uncertain. In the later spectra, after age 100 days, the O I λ7771 profile seems to have

similar, although less prominent, dips. However, neither the spacing nor individual velocities relative to O I λ7771 are the same as in the [O I] $\lambda\lambda$6300, 6364 profile. The O I λ9264 data are much noisier but do not obviously show similar features, nor does the Mg I] λ4571 profile, in which the data are clearer. Because the dips in the [O I] $\lambda\lambda$6300, 6364 profile are not present in the other O I lines or in the Mg I] profile, any explanation of these small features as a result of large-scale asymmetry in the oxygen-emitting region seems unlikely.

Another possibility is that the small-scale features in the [O I] $\lambda\lambda$6300, 6364 profile are produced by absorption or emission from material in the ejecta. In the case of the minimum at 6280 Å, absorption seems an unlikely explanation because the depth of this feature has remained essentially unchanged after more than a year of expansion in which the density and, therefore, the optical depth of the absorber, decreased by a factor of almost 10^5. Nevertheless, absorption attributable to Fe I lines or perhaps absorption in the cool shell formed behind the reverse shock (associated with the circumstellar interaction) remain possible explanations for these features. We have not thoroughly explored the possibility that these features are gaps between narrow emission lines.

8. CONCLUSIONS

From detailed spectrum synthesis calculations, we find good overall agreement between the predictions of the helium star explosion model 4H 47 (Nomoto et al. 1993) and the observed optical spectra of SN 1993J. Model 4H 47 has a helium core mass of 4.0 $M_\odot$ and produces $\sim$0.5 $M_\odot$ of oxygen. Using this model, the observed spectra are best reproduced when the $\sim$0.08 $M_\odot$ of ^{56}Co is macroscopically mixed throughout the inner 0.6 $M_\odot$ of ejecta, significantly reducing the nonthermal energy deposited in the iron core material. Mixing of ^{56}Co into the helium mantle is not required by the late spectra. On the contrary, if more than $\sim$20% of the nickel is mixed into the He mantle, the flux level in the Fe forest 4000–5500 A is poorly reproduced. Our mixing of iron-rich material out to $\sim$3000 km s^{-1} is consistent with the two-dimensional hydrodynamical calculations by Nomoto et al. (1995).

Less massive helium cores have lower gamma-ray optical depths, absorb too little ^{56}Co decay energy, and tend to underproduce prominent spectral features. This situation becomes more severe when large-scale mixing is included; mixing is expected to be more extensive in low-mass helium cores because of the larger mass ratio between the helium layer and the heavy element layer (Suzuki et al. 1993). Such extensive mixing acts to further dilute the gamma-ray flux incident on much of the ejecta mass, further underproducing the observed optical features.

In particular, helium cores smaller than 4H 47 produce too little oxygen to fit the O I emission lines observed in SN 1993J. Because 3H 30 produced only 0.24 $M_\odot$ of oxygen, the oxygen lines in its spectrum were much weaker than those observed in SN 1993J, independent of the level of mixing. The good agreement between the oxygen lines produced by 4H 47 and those in the observed spectra leads us to conclude that the mass of oxygen in SN 1993J is $\sim$0.5 $M_\odot$.

The mass of hydrogen is constrained by the following arguments. First, hydrogen at low velocities ($\lesssim$5000 km s^{-1}) produces a bright, narrow Hα emission feature which was not observed. Second, hydrogen between $\sim$5000–8500 km s^{-1} or between (1.02–1.57) $\times$ 10^4 km s^{-1} produces an [O I] $\lambda\lambda$6300, 6364 absorption feature which was not observed. Third, the mass of hydrogen deduced from the Hα luminosity observed up to $\sim$350 days is $\sim$0.2 $M_\odot$. Taking all constraints into account, we estimate that the mass of the helium-enriched, H/He envelope is between 0.2–0.4 $M_\odot$, and that the bulk of this material lies between 8500–10,000 km s^{-1}. This is roughly consistent with the estimate of the 0.2 $M_\odot$ envelope deduced by Woosley et al. (1994). We note that Baron, Hauschildt, & Branch (1994) and Baron et al. (1995) require a significantly larger helium abundance, $Y = 0.8$, to fit the earlier photospheric spectra. Swartz et al. (1993) also find a much smaller hydrogen mass, close to 0.04 $M_\odot$, in an outer layer of $\sim$0.4 $M_\odot$.

We cannot determine the helium mass from the luminosity of the observed helium lines because the bulk of the helium probably lies at high velocity ($\gtrsim$5000 km s^{-1}), where it absorbs little gamma-ray energy and produces only relatively weak emission. On the other hand, indirect limits on the helium mass follow from the constraints that sufficient oxygen must be produced by the progenitor star and that, for $\sim 10^{51}$ ergs kinetic energy released in the explosion, the expansion velocity must be consistent with the observed line widths. The helium mass of $\sim$2 $M_\odot$ produced in model 4H 47 is consistent with these constraints.

In general, our spectral models are consistent with the binary progenitor models inferred from light curves of Shigeyama et al. (1994), Woosley et al. (1994), and others. In contrast, the large H/He envelope implied by the single-star model of Höflich, Langer, & Duschinger (1993) is inconsistent with the late spectra. A hydrogen envelope of $\sim$3 $M_\odot$ would greatly overproduce the observed Hα emission between 140–350 days.

Despite the evidence for macroscopic mixing, we find that the late spectra show no evidence for large-scale asymmetries or large blueshifts. Instead, the spectral features previously discussed as evidence for large-scale asymmetries (Spyromilio 1994) are explained more consistently by line blending effects in a spherically symmetric nebula. Nevertheless, small-scale asymmetries, perhaps as a result of inhomogeneity in the nebula, may be present (Matheson et al. 1995).

Finally, we mention the unfortunate lack of infrared data for SN 1993J. SN 1987A clearly demonstrated the potential of the IR lines for both abundance determinations and for line identifications. Figure 10 shows the near-infrared spectrum produced by our best-fit model at age 140 days.

The authors would like to thank Ken'ichi Nomoto, for supplying helium star explosion models, and Cecilia Kozma, for allowing us to use her code for solving the Spencer-Fano equation. Keith Berrington and Anil Pradhan gave useful advice on atomic data and helped us use the OPACITY project database. We would also like to thank Cecilia Kozma, Peter Lundqvist, Ken'ichi Nomoto, and Philip Pinto for enlightening conversations. The anonymous referee provided several useful comments and constructive criticism. Our conclusions rely to a great extent on observations made with the William Herschel Telescope operated on the island of La Palma by the Royal Greenwich Observatory in the Spanish Observatorio del Roque de los Muchachos of the Instituto de Astrofisica de Canarias. We are grateful to Peter Meikle and the La Palma group for establishing the excellent archive of SN 1993J observations. This work was supported by the Göran Gustafsson Foundation for Research in Natural Sciences and Medicine.

APPENDIX

ATOMIC DATA

Recombination rates were taken from the following sources: H I, Osterbrock (1989, p. 80); He I, Almog & Netzer (1989); O I, Escalante & Victor (1992). Unless otherwise mentioned, recombination rates came from the tables of Shull & Van Steenberg (1982), Gould (1978), or Aldrovandi & Péquignot (1973). Recombination rates for Co I–IV were assumed equal to the corresponding rates for Fe I–IV. Accurate data for recombination to excited states of Fe II and Co II do not exist, and unfortunately, the hydrogenic approximation is likely to be inaccurate (Pradhan 1993). In the absence of a better approximation, in most of our calculations we have evenly distributed the excited state recombination among the highest excited terms of Fe II and Co II.

Photoionization cross sections were taken from the following sources: H I, Hummer & Seaton (1963); He I, Koester et al. (1985); O I, Butler & Zeippen (1993); Mg I, Butler et al. (1993); Ca I, Scott, Kingston, & Hibbert (1983); Ca II, Shine & Linsky (1974). Photoionization cross sections for Co I–IV were assumed equal to the corresponding cross sections for Fe I–IV. All other photoionization cross sections were taken from Reilman & Manson (1979).

Collision strengths were taken from the following sources: H I, Callaway, Unnikrishnan, & Oza (1987) and Johnson (1972); C I, Nussbaumer & Rusca (1979) and Hayes & Nussbaumer (1984); C II, Lennon et al. (1985); Mg I, Fabrikant (1974); Si I, Pindzola, Bhatia, & Temkin (1977); Fe II, Pradhan & Zhang (1993). Unless otherwise noted, collision strengths were taken from Mendoza (1983). Collision strengths for Co II involving fine-structure transitions in the ${}^3_aF$ and ${}^3_aP$ terms and transitions between these two terms were estimated following the procedure outlined by Osterbrock, Tran, & Veilleux (1992).

Transition probabilities for iron and cobalt ions were taken from Axelrod (1980), Morton (1991), Nahar (1995), and Nussbaumer & Storey (1988). Probabilities for additional fine-structure transitions were taken from Garstang (1962) (Fe II) and Garstang (1957) (Fe III).

REFERENCES

Aldrovandi, S. M. V., & Péquignot, D. 1973, A&A, 25, 137
Almog, Y., & Netzer, H. 1989, MNRAS, 238, 57
Axelrod, T. S. 1980, Ph.D. thesis, Univ. of California, Santa Cruz
Baron, E., & Hauschildt, P. H. 1995, preprint
Baron, E., Hauschildt, P. H., & Branch, D. 1994, 426, 334
Baron, E., et al. 1995, ApJ, 441, 170
Butler, K., Mendoza, C., & Zeippen, C. J. 1993, J. Phys. B: At. Mol. Opt. Phys., 26, 4409
Butler, K., & Zeippen, C. J. 1993, J. Phys. B: At. Mol. Opt. Phys., in press
Callaway, J., Unnikrishnan, K., & Oza, D. H. 1987, Phys. Rev. A, 36, 2576
Cardelli, J. A., Clayton, G. C., & Mathis, J. S. 1989, ApJ, 345, 245
Carlsson, M. 1993, private communication
Chevalier, R. A., & Fransson, C. 1994, ApJ, 420, 268
Escalante, V., & Victor, G. A. 1992, Planet. Space Sci., 40, 1705
Fabrikant, I. I. 1974, J. Phys. B: At. Mol. Opt. Phys., 7, 91
Filippenko, A. V., Matheson, T., & Barth, A. J. 1994, AJ, 108, 2220
Filippenko, A. V., Matheson, T., & Ho, L. C. 1993, ApJ, 415, L103
Fransson, C. 1994, in Supernovae (Les Houches, Session LIV 1990), ed. J. Audouze, S. Bludman, R. Mochkovitch, & J. Zinn-Justin (New York: Elsevier), 677
Fransson, C., & Chevalier, R. A. 1989, ApJ, 343, 323
Fransson, C., & Houck, J. 1995, in preparation
Fransson, C., Houck, J., & Kozma, C. 1994, in IAU Colloq. 145, Supernovae and Supernova Remnants, ed. R. McCray (Cambridge: Cambridge Univ. Press), in press
Fransson, C., Lundqvist, P., & Chevalier, R. A. 1995, ApJ, in press
Fransson, C., & Sonneborn, G. 1994, in Frontiers of Space and Ground-based Astronomy, ed. W. Wamsteker, M. S. Longair, & Y. Kondo (Dordrecht: Kluwer), 249
Freedman, W. L., et al. 1993, BAAS, 25, 914
Fryxell, B., Arnett, D., & Müller, E. 1991, ApJ, 367, 619
Gould, R. J. 1978, ApJ, 219, 250
Garcia, F. 1993, IAU Circ., No. 5731
Garstang, R. H. 1957, MNRAS, 117, 393
———. 1962, MNRAS, 124, 321
Hashimoto, M., Nomoto, K., & Shigeyama, T. 1989, A&A, 210, L5
Hayes, M. A., & Nussbaumer, H. 1984, A&A, 134, 193
Herant, M., & Benz, W. 1991, ApJ, 370, 81L
———. 1992, ApJ, 387, 294
Höflich, P., Langer, N., & Duschinger, M. 1993, A&A, 275, L29
Hummer, D. G., & Rybicki, G. B. 1985, ApJ, 293, 258
Hummer, D. G., & Seaton, M. J. 1963, MNRAS, 125, 437
Iwamoto, K. 1994, Master's Thesis, Univ. Tokyo
Johnson, L. C. 1972, ApJ, 174, 227
Koester, D., Vauclair, G., Dolez, N., Oke, J. B., & Greenstein, J. L. 1985, A&A, 149, 423
Kozma, C., & Fransson, C. 1991, ApJ, 390, 602
Lennon, D. J., Dufton, P. L., Hibbert, A., & Kingston, A. E. 1985, ApJ, 294, 200
Lewis, J. R., et al.. 1994, MNRAS, 266, 27
Matheson, T., Filippenko, A. V., & Ho, L. C. 1995, BAAS, 26, 1361
Mendoza, C. 1983, in IAU Symp. 103, Planetary Nebulae, ed. D. R. Flower (Dordrecht: Reidel), 143
Mihalas, D. 1978, Stellar Atmospheres (San Francisco: W.H. Freeman)
Morton, D. C. 1991, ApJS, 77, 119
Nahar, S. 1995, A&A, 293, 967
Nomoto, K., Iwamoto, K., & Suzuki, T. 1995, Phys. Rep., in press
Nomoto, K., Suzuki, T., Shigeyama, T., Kumagai, S., Yamaoka, H., & Saio, H. 1993, Nature, 364, 6437, 507
Nussbaumer, H., & Rusca, C. 1979, A&A, 72, 129
Nussbaumer, H., & Storey, P. J. 1988, A&A, 200, L25
Osterbrock, D. E. 1989, Astrophysics of Gaseous Nebulae and Active Galactic Nuclei (Mill Valley: University Science Books)
Osterbrock, D. E., Tran, H. D., & Veilleux, S. 1992, ApJ, 389, 305
Patat, F., Chugai, N., & Mazzali, A. 1995, A&A, in press
Pindzola, M. S., Bhatia, A. K., & Temkin, A. 1977, Phys. Rev. A, 15, 35
Podsiadlowski, Ph., Hsu, J. J. L., Joss, P. C., & Ross, R. R. 1993, Nature, 364, 509
Pradhan, A. K. 1993, private communication
Pradhan, A. K., & Zhang, H. L. 1993, ApJ, 409, L77
Reilman, R. F., & Manson, S. T. 1979, ApJS, 40, 815
Scott,P., Kingston, A. E., & Hibbert, A. 1983, J. Phys. B, 16, 3945
Seaton, M. J. 1962, Proc. Phys. Soc. London, 79, 1105
Shibizaki, N., & Ebisuzaki, T. 1988, ApJ, 327, L9
Shigeyama, T., & Nomoto, K. 1990, 360, 242
Shigeyama, T., Suzuki, T., Kumagai, S., & Nomoto, K. 1994, ApJ, 420, 341
Shine, R. A., & Linsky, J. L. 1974, Sol. Phys., 39, 49
Shull, J. M., & Van Steenberg, M. 1982, ApJS, 48, 95
Smith, P. 1993, IAU Circ., No. 5776
Spyromilio, J. 1994, MNRAS, 266, 61
Spyromilio, J., & Pinto, P. A. 1991, in Proc. ESO/EIPC Workshop on SN 1987A and Other Supernovae, ed. I. J. Danziger & K. Kjär (Garching: ESO), 423
Suzuki, T., Kumagai, S., Shigeyama, T., Nomoto, K., Hashimoto, M., & Thielemann, F.-K. 1993, in IAU Colloq. 145, Supernovae & Supernova Remnants, ed. R. McCray & Z. Wang (Cambridge: Cambridge Univ. Press), in press
Swartz, D. A. 1990, A&A, 239, 227
Swartz, D. A., Clocchiatti, A., Benjamin, R., Lester, D. F., & Wheeler, J. C. 1993, Nature, 365, 232
Swartz, D. A., Sutherland, P. G., & Harkness, R. P. 1995, preprint
Trammell, S. R., Hines, D. C., & Wheeler, J. C. 1993, ApJ, 414, L21
Wang, L., & Hu, J. Y. 1994, Nature, 369, 380
Wang, L., Hu, J. Y., Li, A. G., & Li, H. B. 1993, IAU Circ., No. 5847
Wheeler, J. C., & Filippenko, A. V. 1993, preprint
Wheeler, J. C., et al. 1993, ApJ, 417, L71
Woosley, S. E. 1988, ApJ, 330, 218
Woosley, S. E., Eastman, R. G., Weaver, T. A., & Pinto, P. A. 1994, ApJ, 429, 300
Xu, Y., & McCray, R., Oliva, E., & Randich, S. 1992, ApJ, 386, 181